

Geochemistry, Geophysics, Geosystems®




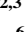







RESEARCH ARTICLE

10.1029/2023GC011386

Experimental Observation of a New Attenuation Mechanism in *hcp*-Metals That May Operate in the Earth's Inner Core

Key Points:

- Zinc, a low pressure analog for *hcp*-iron, deforms by internal stress superplasticity during small amplitude sinusoidal-strain deformation
- Internal stress superplasticity due to mechanical oscillations has not been previously reported
- Internal stress superplasticity is another attenuation mechanism that could be active in the Earth's inner-core

Simon A. Hunt¹ , Andrew M. Walker^{2,3} , Oliver T. Lord⁴ , Stephen Stackhouse² , Lewis Schardong⁵ , Lora S. Armstrong⁶ , Andrew J. Parsons⁷ , Geoffrey E. Lloyd² , John Wheeler⁸ , Danielle M. Fenech⁹ , Stefan Michalik¹⁰ , and Matthew L. Whitaker¹¹ 

¹Department of Materials, University of Manchester, Manchester, UK, ²School of Earth and Environment, University of Leeds, Leeds, UK, ³Department of Earth Sciences, University of Oxford, Oxford, UK, ⁴School of Earth Sciences, University of Bristol, Bristol, UK, ⁵The Geological Survey of Israel, Jerusalem, Israel, ⁶Faculty of Civil Engineering and Geosciences, TU Delft, Delft, The Netherlands, ⁷School of Geography, Earth and Environmental Sciences, University of Plymouth, Plymouth, UK, ⁸School of Environmental Sciences, Jane Herdman Laboratories, University of Liverpool, Liverpool, UK, ⁹Department of Physics, Cavendish Laboratory, University of Cambridge, Cambridge, UK, ¹⁰Diamond Light Source Ltd., Harwell Science and Innovation Campus, Didcot, UK, ¹¹Department of Geosciences, Mineral Physics Institute, Stony Brook University, Stony Brook, NY, USA

Supporting Information:

Supporting Information may be found in the online version of this article.

Correspondence to:

S. A. Hunt,
simon.hunt@manchester.ac.uk

Citation:

Hunt, S. A., Walker, A. M., Lord, O. T., Stackhouse, S., Schardong, L., Armstrong, L. S., et al. (2024). Experimental observation of a new attenuation mechanism in *hcp*-metals that may operate in the Earth's inner core. *Geochemistry, Geophysics, Geosystems*, 25, e2023GC011386. <https://doi.org/10.1029/2023GC011386>

Received 11 DEC 2023

Accepted 12 JUN 2024

Author Contributions:

Conceptualization: Simon A. Hunt, Andrew M. Walker

Data curation: Simon A. Hunt

Formal analysis: Simon A. Hunt

Investigation: Simon A. Hunt, Andrew M. Walker, Oliver T. Lord, Stephen Stackhouse, Lewis Schardong, Lora S. Armstrong, Andrew J. Parsons, Geoffrey E. Lloyd, John Wheeler, Danielle M. Fenech, Stefan Michalik, Matthew L. Whitaker

Methodology: Simon A. Hunt, Andrew M. Walker

Resources: Simon A. Hunt

Abstract Seismic observations show the Earth's inner core has significant and unexplained variation in seismic attenuation with position, depth and direction. Interpreting these observations is difficult without knowledge of the visco- or anelastic dissipation processes active in iron under inner core conditions. Here, a previously unconsidered attenuation mechanism is observed in zinc, a low pressure analog of *hcp*-iron, during small strain sinusoidal deformation experiments. The experiments were performed in a deformation-DIA combined with X-radiography, at seismic frequencies (~ 0.003 – 0.1 Hz), high pressure and temperatures up to $\sim 80\%$ of melting temperature. Significant dissipation ($0.077 \leq Q^{-1}(\omega) \leq 0.488$) is observed along with frequency dependent softening of zinc's Young's modulus and an extremely small activation energy for creep (≤ 7 kJ mol⁻¹). In addition, during sinusoidal deformation the original microstructure is replaced by one with a reduced dislocation density and small, uniform, grain size. This combination of behavior collectively reflects a mode of deformation called “internal stress superplasticity”; this deformation mechanism is unique to anisotropic materials and activated by cyclic loading generating large internal stresses. Here we observe a new form of internal stress superplasticity, which we name as “*elastic strain mismatch superplasticity*.” In it the large stresses are caused by the compressional anisotropy. If this mechanism is also active in *hcp*-iron and the Earth's inner-core it will be a contributor to inner-core observed seismic attenuation and constrain the maximum inner-core grain-size to $\lesssim 10$ km.

Plain Language Summary The Earth's inner-core is the most remote and inaccessible part of our planet. Knowledge of the inner-core's structure comes from interpretation of the information held in seismic waves that have passed through the inner-core. These waves show measurable variation in wave speed and damping with depth. To investigate the wave damping in the inner-core we performed experiments that mimicked the passage of seismic waves through zinc. Zinc was used as a low-pressure analog because it has the same crystallographic structure as the iron in the inner-core. In these experiments, we observed new behavior in the zinc samples that can only be explained by the behavior of different directions within the zinc crystal lattice. These we named “*elastic strain mismatch superplasticity*” and if the same phenomena occurs in the Earth's inner-core it could explain the seismic observations.

1. Introduction

The Earth's solid inner core is the most remote and inaccessible part of our planet. Information encoded in the structure and composition of the inner core during its early solidification could reveal the timing and nature of the onset of Earth's protective magnetic field, generated by convection in the liquid outer core, or even of changes in the way the mantle convects and drives surface dynamics (e.g., Aubert et al., 2008).

The inner-core exhibits depth and azimuthal variation in both seismic wave speed (Deuss, 2014; Irving & Deuss, 2011; Lythgoe et al., 2014; Niu & Wen, 2001; Sumita & Bergman, 2015; Woodhouse et al., 1986) and attenuation (e.g., Yu & Wen, 2006). The attenuation has both hemispherical (Cao & Romanowicz, 2004) and

© 2024 The Author(s). Geochemistry, Geophysics, Geosystems published by Wiley Periodicals LLC on behalf of American Geophysical Union.

This is an open access article under the terms of the Creative Commons

Attribution License, which permits use, distribution and reproduction in any medium, provided the original work is properly cited.

Writing – original draft: Simon A. Hunt, Andrew M. Walker

Writing – review & editing: Simon A. Hunt, Andrew M. Walker, Oliver T. Lord, Andrew J. Parsons, John Wheeler

depth variations (Suda & Fukao, 1990). Attenuation is parametrized as the seismic quality factor, Q , which can be thought of as the efficiency with which wave energy is transmitted. Using body waves (typical frequency 0.5–1.5 Hz), Q has been estimated to be ~ 200 just below the inner core boundary increasing to 1,000–2,000 at the center of the Earth (Doornbos, 1974). Significant regional variation in Q has been found to exist by Pejić et al. (2019) and Li and Cormier (2002), with a global mean $Q_{1 \text{ Hz}} \sim 300$. Using normal modes (frequency < 10 mHz), Mäkinen et al. (2014) showed that attenuation in the inner core is directionally dependent with the North-South direction being both seismically faster and more attenuating than radial directions. The attenuation mechanism(s) in the inner-core is unknown. Postulated mechanisms include: the flow of trapped fluids (Fearn et al., 1981; Singh et al., 2000); diffusion-, dislocation- or elastically accommodated grain-boundary sliding (Jackson et al., 2000); and Zener relaxation, in which Fe atoms switch positions with vacancies and/or solute atoms as a result of the stress imparted by passing seismic waves (Mäkinen et al., 2014).

The inner-core is very close to its melting temperature and the iron from which it is formed is widely accepted to be the *hcp* structure stable above 10 GPa (e.g., Tateno et al., 2010), albeit diluted by light elements (Antonangeli et al., 2010, 2018; Bazhanova et al., 2017; Caracas, 2015; Fei et al., 2016; Fiquet et al., 2001; Li et al., 2018; Mao et al., 2012; Prescher et al., 2015; Sakamaki et al., 2016; Tagawa et al., 2016; Tateno et al., 2012, 2015). However, the experimental data needed to distinguish between potential inner core attenuation mechanisms does not exist because of the extreme conditions under which *hcp*-iron is stable. Deformation experiments on *hcp*-iron are limited to 1000 K and 30 GPa ($T/T_m \sim 0.4$; where T is the temperature and T_m is the melting temperature, both in Kelvins, Merkel et al., 2004; Nishihara et al., 2023). The most recent study of the anelasticity of iron (Jackson et al., 2000) is limited to low pressures where iron adopts the body centered cubic (*bcc*) and face centered cubic (*fcc*) structures.

To account for the limitations of pressures and temperatures that can be replicated in experimental settings, low-pressure *hcp* analogs including zinc, titanium, magnesium and cobalt have been utilized as analogs for the inner core (Bergman et al., 2018; Kanitpanyacharoen et al., 2012). But even on analogs, experiments at high-homologous temperatures are rare (e.g., Bergman et al., 2018) and most studies are performed at low pressures and homologous temperatures (e.g., Jackson et al., 2000). Small amplitude, mechanical oscillation experiments performed on *hcp* metals at ambient pressure are generally at much higher frequencies than seismic waves (Aning et al., 1982; Takahashi, 1952; Wuttig et al., 1981), or infer dissipation from large strain creep tests (Li & Wagoner, 2021). The few mechanical studies at seismic frequencies attribute attenuation, at ambient pressure and low temperatures, in zinc to dislocation motion (Roberts & Brown, 1962). In general though, seismological, experimental and computational studies investigating inner core properties and chemistry, implicitly assume an absence of visco- or anelastic attenuation.

Both seismologically and experimentally, attenuation, Q^{-1} , is the inverse of the quality factor, Q , and is characterized by the loss of amplitude and energy of a wave as it passes through an imperfectly elastic medium. Under forced constant amplitude experiments Q^{-1} manifests as a phase lag between an applied stress and the strain response. It is an inherent property of anelastic and viscoelastic materials and arises due to the time dependent response to applied stress (Nowick & Berry, 1972). An undamped oscillator with no attenuation or energy loss has $Q^{-1} = 0$ ($Q = \infty$) and indicates an elastic (i.e., instantaneous and recoverable) response to stress. A finite Q indicates the operation of plastic strains, requiring time to manifest, that are unrecoverable. Each viscoelastic attenuation mechanism has characteristic frequency and amplitude dependent behaviors which are dependent on the temperature, pressure and microstructure of the sample. The microstructure in turn reflects the deformation and crystallization history of the sample. Comparison between a broad set of experimental results and seismic observations of dispersion (variation of wave velocity with frequency) and intrinsic attenuation (reduction in wave amplitude with distance) is therefore needed to understand attenuation in the Earth's inner-core.

In this contribution, we show how attenuation and microstructural data from *hcp*-zinc give new insights into inner core attenuation via a new mechanical model for grain scale behavior. We measure the viscoelastic response of zinc, to sinusoidal loading, at high pressure and T/T_m up to 0.8; measure the microstructures of the recovered samples; interpret this data to understand the attenuation mechanisms active during small strain deformation and discuss its potential implications for the inner-core.

Table 1
Summary of Samples Discussed in This Study and Their Microstructures

Sample	Experiment	Methods and discussion corresponding to sample	Microstructure		
			Grain-size (μm^2)	WBVI (μm^{-1})	Neighbor versus. random pair
Drawn Wire	As supplied	Main text	3,695	0.0013	Similar
Wire, compressed	Cold compression	Text S3 in Supporting Information S1, main text	891	0.0108	Different
Wire, annealed	High-pressure annealing	Text S3 in Supporting Information S1, main text	1,690	0.0095	Similar
Wire, sinusoidal	Sinusoidal deformation	main text	78	0.0041	Similar
Wire, deformed	Constant strain-rate, step-wise deformation	Text S4 in Supporting Information S1, main text	2,731	0.0134	Different
Powder, compressed	Cold compression	Text S3 in Supporting Information S1, main text	85	0.0130	Different
Powder, sinusoidal	Sinusoidal deformation	Text S2 in Supporting Information S1, main text	138	0.0073	Similar
Powder, deformed	Constant strain-rate, step-wise deformation	Text S4 in Supporting Information S1	400	0.0143	Similar

Note. The first column gives the names the samples are referred to in the text. The reported grain-sizes and WBVI values are the mean of the values plotted in Figure 6 and Figure S6 in Supporting Information S1.

2. Experimental Procedure

The response of zinc relative to an elastic standard under small-amplitude sinusoidal loading, was measured using the experimental method of Li and Weidner (2007). Sinusoidal strains were applied to an experimental column consisting of a zinc sample and corundum elastic standard, whilst simultaneously acquiring X-radiographic images. Axial strains in the sample and elastic standard were determined by tracking displacement of marker foils in the X-radiographs. Strain in an elastic standard is used as a proxy for applied stress, which combined with the sample strain and phase lag of the sample relative to that of the elastic standard, is sufficient to determine the viscoelastic response of the sample. This has been quantified with a multi-parameter viscoelastic model and the recovered samples analyzed for their microstructures to constrain their grain-scale deformation mechanisms.

The main text discusses the sinusoidal deformation experiments on a zinc wire and powder. For brevity, the microstructure figures in the main text are those for the wire sample and equivalent figures for the powder are in Supporting Information S1. Further experiments exploring how sample history and experimental conditions affect microstructure are discussed in Supporting Information S1 and listed in Table 1.

2.1. Samples

The wire sample was taken from a 1 mm diameter high-purity zinc wire (99.9985% metal basis, Puratronic from Alfa Aesar). Samples were prepared by polishing to ~ 1 – 1.3 mm lengths, with flat parallel ends.

Powder samples were made from fine-grained zinc powder (Sigma Aldrich, 99% metal basis, $75 \mu\text{m}$ particle size, that had not been stored in an inert atmosphere). High-resolution X-ray diffraction of the zinc powder shows it to contain trace amounts of two forms of ZnO (cubic and hexagonal) and at least one form of $\text{Zn}(\text{OH})_2$. The powder was pressed into ~ 1 mm long, 1 mm diameter pellets in a steel die with flat-ended pins.

The elastic standards were 1 mm diameter solid rods of Alsint-23 corundum, from Alfa Aesar. Each piece was polished to < 0.9 mm long with flat parallel ends. Two pieces were used on either end of the zinc samples in the sinusoidal deformation experiments to keep the cell symmetrical. Disks of $25 \mu\text{m}$ thick platinum foil were used as markers between the samples and corundum standards as well as at the outer ends of the corundum standards.

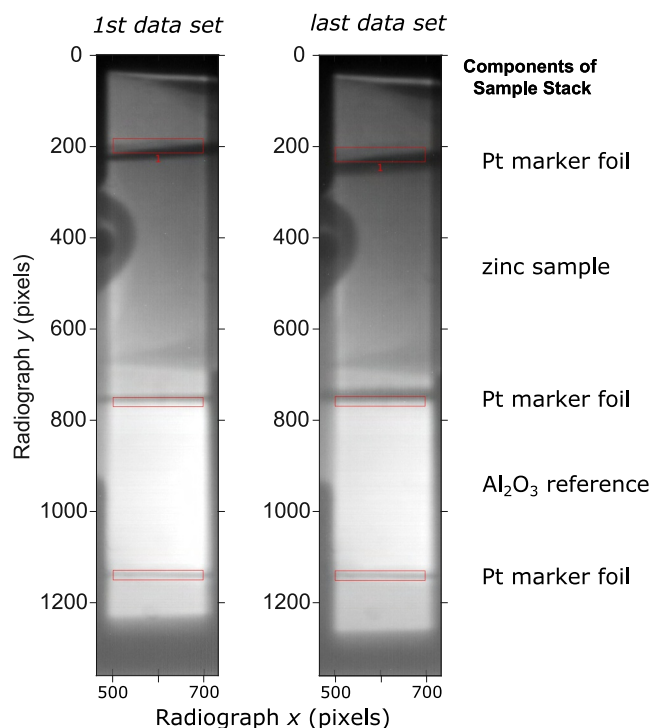


Figure 1. Example X-radiographs, from the (left) beginning and (right) end of the wire experiment. They were acquired at (left) 4.8 GPa and 25°C and (right) 3.3 GPa and 150°C. The radiographs show both the sample and corundum standard, as annotated on the right hand side. The red boxes are the positions of the regions of interest tracked between images. The dark stripes at either side of the images are the shadows of the tungsten carbide anvils. The scale of the image is 2 $\mu\text{m}/\text{pixel}$.

2.2. Sinusoidal Deformation Experiments

The viscoelasticity experiments were performed in the D-DIA (Durham et al., 2002; Wang et al., 2003) on beamline X17B2 at the NSLS, Brookhaven National Laboratory, New York with a white X-ray beam. Diffraction measurements were acquired using a 10-element energy dispersive X-ray diffraction detector (Weidner et al., 2010) which was calibrated using a corundum standard.

The experimental assembly consisted of a 6.1 mm cube of pyrophyllite baked to 1000°C with a 3.0 mm hole drilled through it normal to one face. Into this was placed, a crushable alumina sleeve (3.0 mm outer, 2.36 mm inner diameter), a graphite furnace (2.36 mm outer, 2.10 mm inner diameter, 6.1 mm long), and a boron nitride sleeve (1.8 mm outer diameter, 1.0 mm inner diameter, 3.0 mm long). A sample stack, consisting of a zinc sample bracketed by two corundum pistons, was inserted into this boron nitride sleeve and the remaining space filled by crushable alumina. A C-type thermocouple inside a 0.8 mm diameter 4-bore alumina rod was inserted radially with its hot junction just inside the furnace but not touching the sample. A cross-section of the cell assembly is shown in Figure S2 (Supporting Information S1).

The experiment was pressurized to the desired end-load over ~ 2 hr. At pressure, diffraction patterns were acquired from both sample and standard. The zinc diffraction volume was in the center of the sample and that of the corundum in the part closest to the zinc. The samples were then strained sinusoidally, with the smallest resolvable strains, at periods of 10, 30, 100, and 300 s by driving the D-DIA's deformation pumps. During deformation, X-radiographs (e.g., Figure 1) were acquired using a yttrium aluminum garnet scintillator and a visible-light camera, for 10 nominal periods, at a rate of 20 or 40 images per period.

For all but the 300 s data, two full cycles were allowed to elapse before data collection was started allowing the system to reach a mechanical equilibrium. After all data had been acquired at each temperature, the temperature was changed and the cycle repeated. Data was acquired during both increasing and decreasing temperature steps, to confirm that the results are not affected by the thermal history of the sample. During sinusoidal deformation, the total end-load on the system was kept constant, minimizing any changes in pressure applied to the sample. Experiments were ended by simultaneously stopping the sinusoidal deformation and quenching the temperature. After the experiment had cooled to room temperature, the end load was reduced over a few hours while the position of the deformation rams was held constant, to prevent further deformation of the samples.

2.3. Pressure Determination

The pressure ($P = \text{volume strain} \times \text{bulk modulus}$), in the sinusoidal deformation experiment was calculated from the energy dispersive corundum diffraction patterns. Although zinc is more compressible and should give more precise pressure estimates, above $\sim 200^\circ\text{C}$ its diffraction patterns ceased to reliably contain enough diffraction peaks to reliably determine volume strains. Any individual peaks would rapidly increase and decrease in relative intensity, as the zinc underwent rapid recrystallization. Therefore the distinguishable corundum diffraction peaks were fit using the software package “Plot85” and an independent unit cell volumes calculated for each of the detector elements. Volume strains were calculated independently for each of the detector element using the corresponding open-press unit cell volume, the corundum thermal expansion coefficients of Fei (1995) and the temperature reported by the thermocouple.

Pressures were calculated, from the volume strain, assuming a bulk modulus of $K_0 = 254.28$ GPa along with pressure and temperature derivatives of $K' (= \partial K / \partial P) = 4.27$ and $\partial K / \partial T = -0.0173$ GPa K^{-1} respectively. The bulk modulus and the temperature derivative are a linear fit to the Voigt-Reuss-Hill bulk moduli calculated

using MSAT (the Matlab Seismic Anisotropy Toolbox, Walker & Wookey, 2012) from the elastic stiffnesses (c_{ij}) of Goto et al. (1989). The pressure derivative was calculated from the pressure dependencies of the elastic stiffnesses of Gieske and Barsch (1968) in the same manner, assuming the derivatives are linear at pressures greater than 1 GPa. The pressure reported at each condition are the weighted mean and standard deviation of the values calculated from all the detector elements. Elastic stiffnesses were used, rather than an Equation of State, for internal consistency with subsequent Young's moduli calculations (Section 2.5).

2.4. X-Radiograph Analysis

The X-radiographs were processed using the *FoilTrack* algorithm (Hunt, 2023), which was developed specially for this data set. It was developed because earlier algorithms used to process high strain (Dobson et al., 2012b; Hunt et al., 2009, 2010, 2019) and small-strain cyclic data (Dobson et al., 2008, 2010; Hunt et al., 2011, 2012) were unable to provide sufficiently precise or coherent period, phase or amplitude values for the sample length changes. *FoilTrack* is a digital image correlation algorithm that treats complete series of images as a single, consistent sequence, while accounting for the known deformation applied to the sample. The period, phase and amplitude of the sinusoidal displacement for each region of interest are returned by the algorithm. These can subsequently be used to calculate the sinusoidal phase (Φ) and amplitude (A) of the length change in each sample and reference.

During the experiment, the foil shadows adjacent to the zinc sample became broader as the platinum marker foil diffused into the zinc (Figure 1). To minimize the effect of this on the measurements, the regions of interest were positioned automatically around the marker foils. The regions of interest adjacent to the zinc sample (Figure 1, middle boxes) were centered over the maximum gradient (as interpolated by a spline) on the side of the foil away from the sample. Those not adjacent to the zinc sample (Figure 1, top and bottom red boxes) were centered over the minimum in a spline interpolation of the intensity profile and the width and depth of these remained very similar throughout the experiment. The radiographs exhibit very little change through the experiment (Figure 1) and any inferred changes in samples length are small.

Sample strain caused by the sinusoidal deformation is defined as:

$$\epsilon = A/l \quad (1)$$

where l is the length of the sample in the reference image, corrected for the thickness of the platinum foils.

Assuming the corundum standard is elastic and isotropic, the frequency dependent, relaxed, Young's modulus of the zinc sample is:

$$E_{Zn}(\omega) = \frac{\epsilon_{Al_2O_3}}{\epsilon_{Zn}} E_{Al_2O_3} \quad (2)$$

where ϵ is the sinusoidal strain amplitude (Equation 1) in the sample and reference and $E_{Al_2O_3}$ is the elastic Young's modulus of corundum. For each measurement, the Young's modulus of corundum, $E_{Al_2O_3}$, is the Voigt-Reuss-Hill average of corundum's elastic stiffnesses (c_{ij}), at the temperature of the thermocouple and the pressure calculated from the diffraction (Section 2.3). These calculations were performed using MSAT (Walker & Wookey, 2012) and the same elastic stiffnesses used to determine the pressure (Gieske & Barsch, 1968; Goto et al., 1989).

The strain energy attenuation is (Cooper, 2002):

$$Q^{-1} = \tan(\delta) = \tan(\Phi_{Al_2O_3} - \Phi_{Zn}) \quad (3)$$

where δ is the loss angle and is equal to the difference in phase of the length changes in the corundum standard ($\Phi_{Al_2O_3}$) and zinc sample (Φ_{Zn}) respectively.

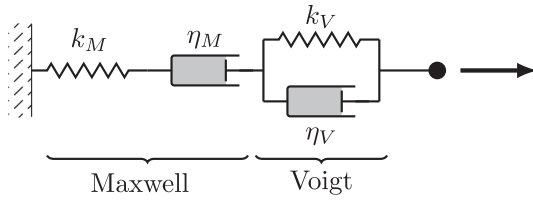


Figure 2. Schematic representations of Burgers models of viscoelasticity. Springs (labeled k) represent the elastic components of the model and dashpots (labeled η) the viscous components; under axial deformation $k_M \equiv E$, the Young's modulus. The Burgers model is formed of Maxwell and Kelvin models in series.

2.5. Viscoelastic Models

The time dependent, unrecoverable, response of viscoelastic media to cyclic deformation can be measured but to explain it a mathematical model is needed. The model must incorporate elasticity but also one or more plastic, dissipative, processes. Such models are constructed from combinations of springs and dashpots (e.g., Figure 2) which, depending on the model, may represent independently measurable properties. Each spring–dashpot model has different frequency-dependent behavior that may also point to particular physical processes occurring in a sample (Banks et al., 2011; Faul & Jackson, 2015; Gribb & Cooper, 1998; Jackson, 2015; Jackson et al., 2000; Lakes, 1999; Nowick & Berry, 1972; Sundberg & Cooper, 2010). The models relate angular frequency, ω ($=2\pi/\text{period}$), and stress, $\sigma(t) = \sigma_0 \exp(i\omega t)$, to the

strain response, $\varepsilon(t) = \varepsilon_0 \exp(i\omega t - \delta)$, by a loss angle, δ . For each model, the strain response can be obtained by integrating its behavior over the stress history to compute the dynamic compliance, $J^*(\omega)$ (Jackson, 2015; Nowick & Berry, 1972). There is no specific spring–dashpot model for internal stress superplasticity. Consequently, a number of viscoelastic models were investigated and the Burgers model was found to best describe the data with physically reasonable values for the parameters.

The Burgers model (Figure 2) is usually expressed in terms of: the unrelaxed compliance, $J_M (=1/k_M)$; the viscoelastic relaxation of the compliance, $J_V (=1/k_V)$; the Maxwell viscosity, η_M ; and the retardation time, τ_V . Where τ is:

$$\tau = \eta/k \quad (4)$$

The frequency dependent Young's modulus, $E(\omega)$ (Equation 2) is the property measured under an axial shortening regime. Substituting the Young's modulus for k , the complex compliance can be expressed in terms of the four independent model components, E_M , η_M , E_V , and η_V (after Jackson, 2015):

$$J^*(\omega) = \frac{1}{E_M} + \frac{1}{E_V(1 + i\omega\eta_V/E_V)} - \frac{i}{\omega\eta_M}$$

Separating the real and imaginary components gives:

$$J_1(\omega) = \frac{1}{E_M} + \frac{1}{E_V(1 + \omega^2\eta_V^2/E_V^2)} \quad (5a)$$

$$J_2(\omega) = \frac{\omega\eta_V}{E_V^2(1 + \omega^2\eta_V^2/E_V^2)} - \frac{1}{\omega\eta_M} \quad (5b)$$

where E_M and E_V are the respective spring constants of the Maxwell and Voigt components of the Burgers model and η_M and η_V are the corresponding dashpot viscosities (Figure 2).

Using the expressions for J_1 and J_2 , the frequency dependent Young's modulus (equivalent to Equation 2) is (e.g., Jackson, 2015):

$$E(\omega) = \sqrt{J_1(\omega)^2 + J_2(\omega)^2} \quad (6)$$

and the strain energy dissipation (equivalent of Equation 3) is:

$$Q^{-1}(\omega) = \frac{J_2(\omega)}{J_1(\omega)}. \quad (7)$$

The Burgers model was fit to the experimental $E(\omega)$ and $Q^{-1}(\omega)$ data (Equations 2 and 3) at each temperature by simultaneously minimizing the unweighted normalized residuals for both $E(\omega)$ and $Q^{-1}(\omega)$ (Equations 6 and 7).

The parameters solved for in the fitting were the period ($=2\pi/\omega$) and the independent elastic (E) and viscous (η) components of the model (Equation 5). Standard errors on each parameter were returned by the least squares difference minimization routine and have been propagated through the analysis as needed.

Equations 5–7 describes the change in sample response with frequency. By assuming negligible pressure derivatives and a functional form for each of the 4 Burger's model parameters, a single description of the data as a function of frequency and pressure can be made of the Burgers model, it was possible to simultaneously fit all the data. A linear temperature dependency was assumed for E_M . The viscosities (η_M and η_V) were assumed to have Arrhenius temperature dependencies ($\ln \eta(T) = a + E_a/RT$) with an activation energy E_a . The temperature dependence of E_V was less clear; a number of possible functions were tested for E_V but an Arrhenius temperature dependence was eventually used because it both approximated the data and remained greater than zero. As with the temperature independent models, standard errors for each parameter of this model were returned by the minimization routine.

2.6. Microstructural Analysis

The experimental samples were mounted in epoxy resin and polished for analysis in the FEI Quanta 650 field emission gun (FEG) scanning electron microscope at the University of Leeds. The final finish was a 0.03 μm colloidal silica chemo-mechanical polish in an alkaline solution (Lloyd, 1987). Electron Back-Scatter Diffraction (EBSD) measurements were obtained using a 20 kV accelerating voltage, a spot size of 65 μm and a working distance of 27 mm. The step size was $\sim 1 \mu\text{m}$ except for an as-purchased wire sample in which it was $\sim 3.54 \mu\text{m}$. The Kikuchi patterns were automatically indexed using Oxford Instrument's AZtec software package. Zinc metal, ZnO, two forms of $\text{Zn}(\text{OH})_2$ and Al_2O_3 were listed as possible phases during indexing.

Grains were reconstructed in MTEX (v5.5.1, Bachmann et al., 2010, 2011) using a 10° misorientation-angle for the grain-boundary threshold. Some of the samples retained significant surface scratching which influences the grain reconstruction. To account for this, data within grains affected by scratches were removed from the analysis and the grain-reconstruction rerun. The twin plane was identified from the annealed wire sample by finding the most common grain-grain misorientation relationships. Twin boundaries were identified in the samples and grains merged if the misorientation between adjacent grains was within 5° of the twin plane.

Proxies for dislocation density and the relationship between neighboring grains were calculated in the form of the Weighted Burgers Vector (WBV, Wheeler et al., 2009) and neighbor-pair and random-pair misorientation distributions (Wheeler et al., 2001) respectively in CrystalScape (v2.1, Wheeler et al., 2009). High angle boundaries, without an organized geometrically necessary dislocation structure, were excluded from WBV calculations using a misorientation threshold of 5° between pixels. Neighbor-pair misorientation angles were calculated for adjacent pixels that are separated by grain-boundaries as defined by the 10° grain-boundary misorientation threshold. Random-pair distributions were calculated, as reference, for misorientations between 10 and 80° ; the upper threshold was utilized to remove the effect of twinning on the distribution comparison.

3. Results

A number of sinusoidal deformation experiments were performed for this study, at up to 4.8 GPa, 400°C and $T/T_m < 0.8$; a full list of the complimentary experiments and samples is in Table 1. For brevity, figures in the main text show the results from wire experiment which exemplify the key results; equivalent figures for the powder sample are included in Supporting Information S1 (Text S2) and are cross-referenced in the main text.

3.1. Sinusoidal Deformation Experiments

The frequency-dependent Young's moduli, $E(\omega)$, decreases with oscillation period (Figure 3a, Figure S3a in Supporting Information S1) and dissipation, $Q^{-1}(\omega)$, increases in a manner consistent with a dissipation peak over a broad background (Figure 3b, Figure S3b in Supporting Information S1). With decreasing period, data shows less attenuation ($Q^{-1}(\omega) \rightarrow 0$ as $\omega \rightarrow \infty$) and the frequency dependent elastic modulus approaches the elastic, infinite frequency, modulus ($E(\omega) \rightarrow E$ as $\omega \rightarrow \infty$). Data collected before and after the maximum temperature do not show significant offsets (open vs. filled symbols, Figure 3, Figure S3 in Supporting Information S1), implying sample history has negligible effect on the measurements. There is no resolvable change in the sinusoidal strain magnitude within any of the sinusoidal measurements. Typical strain amplitudes for both the sample and standard

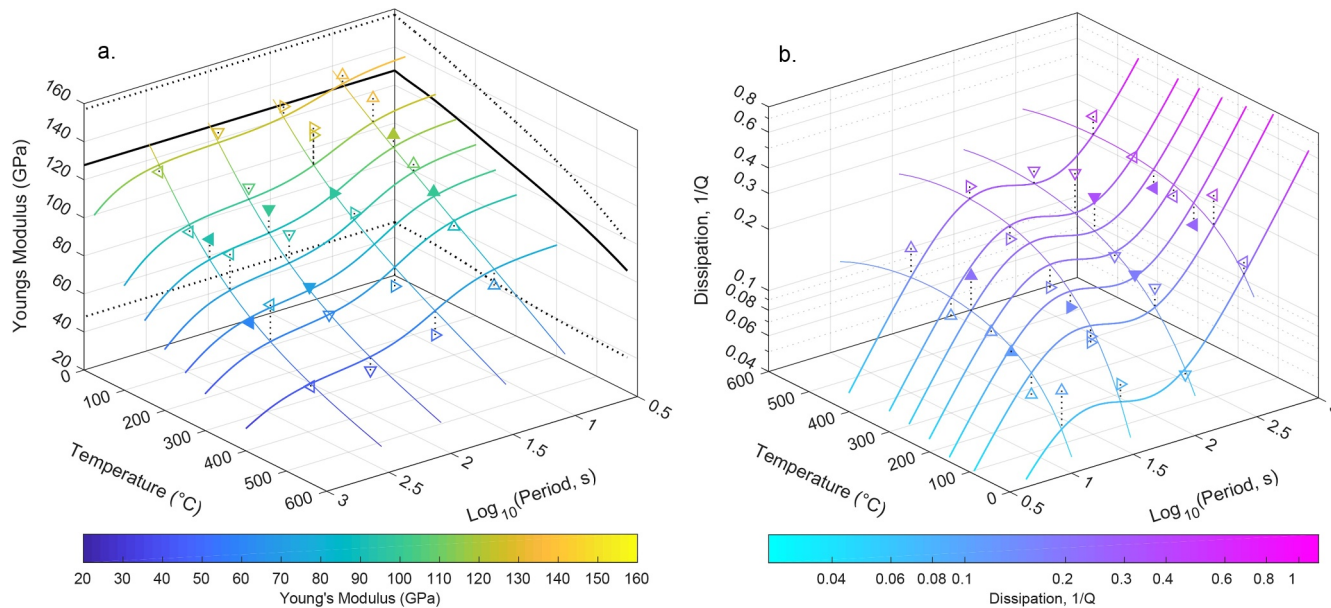


Figure 3. (a) Frequency dependent Young's modulus, $E(\omega)$ (b) dissipation, $Q^{-1}(\omega)$, from the wire sinusoidal deformation experiment; the equivalent plots for the wire sample are in Figure S3 of the Supporting Information S1. The open symbols are the data collected before the maximum temperature of the experiment and the filled symbols after; for the order of the data collection see Table 2. Dotted lines connect the data to the corresponding point in the fitted plane. Error bars have been excluded for clarity; the mean errors in $E(\omega)$ and $Q^{-1}(\omega)$ are 13.9 GPa and 0.03 respectively. The solid lines are the Burgers model fit to all the data and is plotted at the nominal periods and temperatures of the measurements. In (a) the heavy black lines in the back planes are the elastic Young's modulus calculated from a Voigt-Reuss-Hill average of the zinc c_{ij} and the dashed lines are the maximum and minimum possible elastic Young's moduli from the c_{ij} . All lines of constant period terminate at the melting temperature. Note that the directions of the temperature and period axes are reversed between parts (a) and (b).

are $\sim 6 \times 10^{-4}$ and $\sim 10^{-4}$ respectively (Table 2, Table S1 in Supporting Information S1). Strain amplitudes in the corundum standard indicates axial stress amplitudes, in the wire sample, ranging from 22 to 84 MPa, with a mean of 54 MPa.

The absolute $Q^{-1}(\omega)$ values in this study ($0.49 > Q^{-1}(\omega) > 0.05$) are within the range of values reported in other studies of viscoelasticity and are slightly larger than those measured in iron and steel at similar homologous temperatures ($0.33 > Q^{-1}(\omega) > 0.001$; Jackson et al., 2000) but larger than Q^{-1} values determined for the Earth's inner core ($Q^{-1} \lesssim 0.005$, e.g., Doornbos, 1974; Li & Cormier, 2002; Pejić et al., 2019). The range of $Q^{-1}(\omega)$ values here (< 1 log unit) though are smaller than in previous studies which typically range over more than 1.5 log units.

The $E(\omega)$ data fall between the maximum and minimum possible elastic Young's moduli (dashed black lines in Figure 3a, Figure S3a in Supporting Information S1) and are predominantly smaller than the isotropic average elastic Young's moduli (solid black lines in Figure 3a, Figure S3b in Supporting Information S1). The elastic moduli were calculated in MSAT (Walker & Wookey, 2012) for the mean pressure of the experiment from the ambient condition and temperature dependencies of the elastic stiffnesses (c_{ij}) of Alers and Neighbours (1958) and the pressure derivatives of Srinivasan and Rao (1971), as compiled by Ledbetter (1977).

3.2. Viscoelastic Modeling

The Burgers' model was fit to the $E(\omega)$ and $Q^{-1}(\omega)$ data, at each temperature separately (Table 3, symbols in Figure 4). By assuming temperature dependencies for each Burgers model parameter, the entire data set could be fit with a single model (lines in Figure 3, Figures S3 and S4 in Supporting Information S1). The $E(\omega)$ and $Q^{-1}(\omega)$ data, both at individual temperatures and as a whole, are well described by the Burgers model (Figure 3, Figure S3 in Supporting Information S1), which reproduces the dispersion peak or plateaus in $Q^{-1}(\omega)$ and changes in $E(\omega)$ in temperature and period. The fits though, may systemically overestimate the size of the dissipation peak near 30 s in the wire sample (Figure 3) and underestimate it in the powder sample (Figure S3 in Supporting Information S1). This is interpreted as a reflection of differing trade offs in the fitting. The Maxwell relaxation times are all within the experimental periods, while the Voigt retardation times are all smaller than the smallest experimental period

Table 2

Experimental Conditions and Strain Data From the Wire Sample in This Study; for the Powder Sample the Equivalent Values Are in Table S1 of the Supporting Information S1

Group	Temperature (°C)	Pressure (GPa)	Period (s)	Strain amplitude, ϵ			Phase lag zinc-ref (degrees)	$E_{\text{Al}_2\text{O}_3}$ (GPa)	$E(\omega)$ (GPa)	$Q^{-1}(\omega)$
				Zinc ($\epsilon \times 10^6$)	Al_2O_3 ($\epsilon \times 10^6$)					
1	25	4.8(8)	300.010(62)	687(5)	188(7)	12.4(28)	425.4	116(15)	0.22(5)	
			100.437(1)	658(4)	198(5)	4.3(5)		128(12)	0.08(1)	
			29.961(3)	545(2)	168(2)	4.8(12)		131(7)	0.08(2)	
2	100	4.8(8)	10.020(2)	261(2)	84(2)	5.5(18)	422.5	138(10)	0.10(3)	
			299.453(49)	783(5)	172(6)	21.6(25)		93(14)	0.40(5)	
			100.003(1)	693(6)	175(7)	9.6(8)		107(16)	0.17(1)	
			30.200(5)	554(3)	167(3)	6.5(13)		128(7)	0.11(2)	
			30.122(2)	558(2)	164(2)	7.0(9)		124(5)	0.12(2)	
3	200	4.2(4)	9.995(2)	264(2)	84(2)	4.4(17)	414.7	134(9)	0.08(3)	
			299.801(37)	870(4)	193(4)	17.2(17)		92(9)	0.31(3)	
			100.064(1)	820(3)	183(3)	11.0(3)		93(7)	0.19(1)	
			29.891(4)	645(3)	145(3)	9.6(16)		93(9)	0.17(3)	
4	300	4.2(4)	9.977(2)	300(2)	79(2)	7.2(20)	409.4	110(11)	0.13(4)	
			300.021(105)	883(12)	164(11)	21.1(54)		76(28)	0.39(10)	
			100.922(2)	840(4)	125(9)	21.5(17)		61(29)	0.39(3)	
			29.913(3)	675(2)	108(4)	13.1(21)		65(14)	0.23(4)	
5	400	4.1(6)	9.983(2)	308(1)	66(3)	6.9(28)	403.5	87(17)	0.12(5)	
			299.907(65)	922(6)	99(12)	26.0(76)		43(48)	0.49(14)	
			99.372(1)	875(5)	92(8)	17.9(18)		42(35)	0.32(3)	
			29.960(3)	712(2)	89(4)	18.7(25)		51(16)	0.34(5)	
6	250	3.4(6)	10.039(2)	331(2)	55(3)	11.6(32)	408.2	67(20)	0.21(6)	
			300.868(57)	852(7)	127(9)	16.9(48)		61(30)	0.30(9)	
			99.911(1)	823(4)	142(5)	18.6(7)		70(14)	0.34(1)	
7	150	3.3(9)	9.994(2)	307(2)	75(3)	11.9(23)	412.8	100(14)	0.21(4)	
			300.170(245)	802(29)	183(33)	14.1(126)		94(75)	0.25(23)	
			100.343(1)	764(10)	186(10)	10.0(9)		101(22)	0.18(2)	
			30.036(4)	638(4)	152(4)	8.6(17)		98(11)	0.15(3)	
			9.967(2)	308(3)	89(3)	6.4(21)		120(12)	0.11(4)	

Note. The data are presented in the order in which they were collected. The values of $E_{\text{Al}_2\text{O}_3}$ are those used in the calculations and were calculated as described in the text. Numbers in parentheses are the standard error in the last significant figure.

(Table 3), consistent with the observed softening behavior. The coefficients from the single model with the assumed temperature dependencies match those calculated independently at each separate temperature (Figure 4).

The parameters returned by the independent fits at each temperature have physically reasonable values (Table 3) and vary systematically with temperature (Figure 4). Alternative viscoelastic models do not replicate the features of the data, or do so with physically unreasonable parameters. Two component models of viscoelasticity (i.e., Maxwell or Voigt models, Figure 2) are unable to reproduce gradient changes in $Q^{-1}(\omega)$ data (Faul & Jackson, 2015) and require frequency dependent viscosities. The Andrade model (Cooper, 2002; Sundberg & Cooper, 2010) produces physically unreasonable parameters; the model's "micro-creep coefficient" returned fitted values >200 . Much greater than the accepted value of $\sim 1/3$, which has been observed both in zinc (Cottrell & Aytakin, 1947) and other materials (Sundberg & Cooper, 2010). The limited number of periods prevented fitting more models with more parameters, for example, Extended Burgers' model (Jackson, 2015).

Over both experiments there is a substantial reduction in pressure (Table 2, Table S1 in Supporting Information S1) but there is no significant offset between the $E(\omega)$ and $Q^{-1}(\omega)$ values, from before and after the maximum

Table 3
Burgers Model Fits to the Data for Each Temperature Condition

Group	Temperature (°C)	Pressure (GPa)	Burgers' model parameters				Relaxation time τ_M (s)	Retardation time τ_V (s)
			E_M (GPa)	η_M (10^3 GPa s)	E_V (GPa)	η_V (GPa s)		
Wire sample								
1	25	4.8 ± 0.8	149 ± 10	30.9 ± 2.3	729 ± 80	1,342 ± 310	208 ± 16	1.8 ± 0.4
2	100	4.8 ± 0.8	129 ± 3	13.1 ± 0.8	741 ± 49	2,933 ± 351	101 ± 6	4.0 ± 0.5
3	200	4.2 ± 0.4	120 ± 4	13.8 ± 0.8	344 ± 19	1,566 ± 139	115 ± 7	4.6 ± 0.4
4	300	4.2 ± 0.4	93 ± 9	7.9 ± 1.9	163 ± 39	1,557 ± 425	85 ± 21	9.5 ± 2.6
5	400	4.1 ± 0.6	76 ± 4	4.5 ± 0.3	104 ± 10	575 ± 90	60 ± 5	5.5 ± 0.9
6	250	3.4 ± 0.6	117 ± 6	12.0 ± 1.9	119 ± 12	956 ± 98	102 ± 17	8.0 ± 0.9
7	150	3.3 ± 0.9	123 ± 7	17.9 ± 1.5	382 ± 27	1,869 ± 185	145 ± 12	4.9 ± 0.5
Powder sample								
1	28	2.6 ± 0.6	127 ± 2	29.1 ± 3.7	818 ± 51	4,026 ± 266	230 ± 29	4.9 ± 0.3
2	182	3.7 ± 0.7	121 ± 5	10.1 ± 1.7	338 ± 35	1,113 ± 289	84 ± 14	3.3 ± 0.9
3	227	3.6 ± 1.5	96 ± 1	9.1 ± 2.1	382 ± 100	3,961 ± 302	95 ± 22	10.4 ± 0.8
4	279	3.7 ± 0.5	108 ± 3	12.0 ± 1.9	364 ± 28	1,521 ± 186	111 ± 18	4.2 ± 0.5
5	325	3.5 ± 0.7	100 ± 5	$3.7 \times 10^8 \pm 0.0$	151 ± 18	2,833 ± 181	$3.7 \times 10^9 \pm 8.5 \times 10^7$	18.8 ± 1.3
6	377	3.4 ± 0.4	94 ± 3	8.8 ± 3.0	303 ± 77	2,269 ± 234	94 ± 32	7.5 ± 0.8
7	34	2.5 ± 0.6	132 ± 4	12.6 ± 3.0	575 ± 120	3,844 ± 375	95 ± 23	6.7 ± 0.7
8	256	2.7 ± 3.6	114 ± 5	4.7 ± 0.9	733 ± 158	1,329 ± 743	41 ± 8	1.8 ± 1.0
9	120	2.9 ± 0.8	122 ± 1	18.7 ± 0.6	1,082 ± 53	3,248 ± 488	154 ± 5	3.0 ± 0.5

Note. The values are plotted in Figure 4. The errors on the values are those reported by the minimization algorithm used for the fitting. The relaxation and retardation times were calculated using Equation 4.

temperature in each experiment (open vs. filled symbols in Figure 3, Figure S3 in Supporting Information S1). Nor is there any robust difference in Burgers' model parameters (Figure 4). Sample history and the relatively large pressure change over the experiment do not therefore exert meaningful influence on the measured values.

For both the wire and the powder, the predicted E_M show very good agreement with those expected for a random orientation (Figure 4a). The calculated $\partial E_M / \partial T$ values are within 1.5 standard errors of each other and within two standard errors of previous elastic measurements' temperature derivatives (Figure 4, Table 4). The value of $\partial E_M / \partial T$ from the wire is greater than that expected from the previous elastic measurements, this is likely due to the minor geometrical imperfection of the sample.

The creep viscosities, η_M , for the wire and powder agree with each other but poorly with values from previous deformation studies (Figure 4b). They are significantly less temperature dependent than previous dislocation creep experiments (Figure 4; Murthy & Sastry, 1982; Tegart & Sherby, 1958) but are always much greater than the superplastic viscosity of zinc ($\eta < 2,700$ GPa s above 200 K, Kitazono et al., 2001; Wu et al., 1987).

The activation energy for creep (E_{a,η_M}) in the wire is 6.8 ± 1.1 kJ/mol and in the powder is 4.2 ± 2.0 kJ/mol. These values are within 1.2 standard errors of each other and are significantly smaller than the activation energies for creep by dislocation climb or basal slip in zinc (88 and 159 kJ/mol respectively, Tegart & Sherby, 1958), self-diffusion (91.3–101.7 kJ/mol, Chabildas & Gilder, 1972; Shirn et al., 1953), grain boundary diffusion (60.7 kJ/mol, Wajda, 1954), twinning (29.7 ± 10 kJ/mol, Cooper & Washburn, 1967) or grain boundary sliding (40–100 kJ/mol, Watanabe et al., 1984). Instead they are closer to consistency with the low activation energy for creep observed by Matsunaga et al. (2010) and Roth et al. (1974) and models of internal stress superplastic creep (Kitazono, Hirasaka, et al., 1999; Kitazono, Sato, & Kuribayashi, 1999; Kitazono et al., 2001; Wu et al., 1987). The studies referenced here were made with temperatures ranges of 100–300°C and mostly with a maximum temperature below 350°C. The temperature range in this study is more than 25% larger and our maximum temperature is higher, reinforcing the robustness and unusualness of our activation energies.

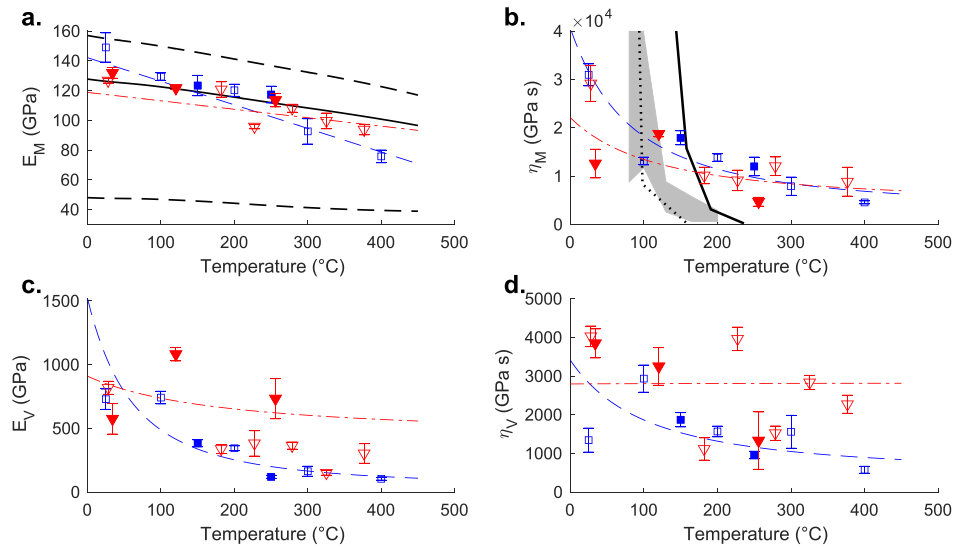


Figure 4. Burgers model parameters plotted against temperature for the wire (blue squares) and powder (red triangles) samples: (a) Maxwell Young's modulus, E_M ; (b) Maxwell viscosity, η_M ; (c) Voigt elastic modulus, E_V ; and the Voigt viscosity, η_V (see Equation 5, Figure 2). The symbols are the Burgers fit to the data at each temperature only; the open symbols are the data collected before the maximum temperature of the experiment and the filled symbols after. Lines are from the fit to all the data assuming the temperature derivatives listed in Table 4; they are not fits to the symbols. In (a): the solid black line is the isotropic elastic Young's modulus of zinc at the average pressure of the wire experiment (4.1 GPa) and the dashed lines are the maximum and minimum possible elastic Young's moduli calculated in MSAT (Walker & Wookey, 2012). In (b): the solid black line, dashed black line and gray area are viscosities ($\eta = \sigma/\dot{\epsilon}$) derived from the experiments in dislocation-controlled creep regimes by Tegart and Sherby (1958), Thompson (1955), and Murthy and Sastry (1982) respectively. There are no comparable previous measurements for parts (c) and (d).

The functional forms of the Voigt elements of the model (Figures 4c and 4d) are less clear than those of the Maxwell elements, due to greater scatter of the Burgers model parameters. Although the values from each sample overlap, the agreement between these is not as good as those of the Maxwell components and this may be due to subtle differences between the samples. The physical processes behind E_V and η_V are not clear and any interpretation requires assumptions about or knowledge of the dissipation mechanism. This prevents any comparison with previous measurements.

3.3. Experimental Microstructures

The Burgers model does not of itself identify the dissipation mechanism active in the experiments. Understanding the viscoelastic dissipation mechanism therefore requires understanding any microstructural differences between the sinusoidally deformed samples and the other deformation states produced during our experiments (Table 1).

Table 4
Temperature Dependent Burgers Model Parameters Fit to $E(\omega)$ and $Q^{-1}(\omega)$

Constant	Wire		Powder	
	Intercept (p_0)	Slope (p')	Intercept (p_0)	Slope (p')
$E_M = p_0 + p' \cdot T$	$142.1 \pm 12.8 \text{ GPa}$	$-0.159 \pm 0.038 \text{ GPa K}^{-1}$	$118.7 \pm 19.7 \text{ GPa}$	$-0.057 \pm 0.076 \text{ GPa K}^{-1}$
$\eta_M = \exp(p_0 + p'/R(T + 273))$	7.6 ± 0.3	$6,803 \pm 1,052 \text{ J mol}^{-1} \text{ K}^{-1}$	8.1 ± 0.6	$4,206 \pm 1,954 \text{ J mol}^{-1} \text{ K}^{-1}$
$E_V = \exp(p_0 + p'/R(T + 273))$	3.1 ± 0.2	$1,158 \pm 104 \text{ J mol}^{-1} \text{ K}^{-1}$	6.0 ± 0.6	$215 \pm 252 \text{ J mol}^{-1} \text{ K}^{-1}$
$\eta_V = \exp(p_0 + p'/R(T + 273))$	5.9 ± 0.2	$5,117 \pm 974 \text{ J mol}^{-1} \text{ K}^{-1}$	7.9 ± 0.5	$-23 \pm 1,849 \text{ J mol}^{-1} \text{ K}^{-1}$

Note. These values are derived from the measurements in Table 2. The models are plotted in Figure 3, Figure S3 in Supporting Information S1 and compared to the independent temperature fits in Figure 4.

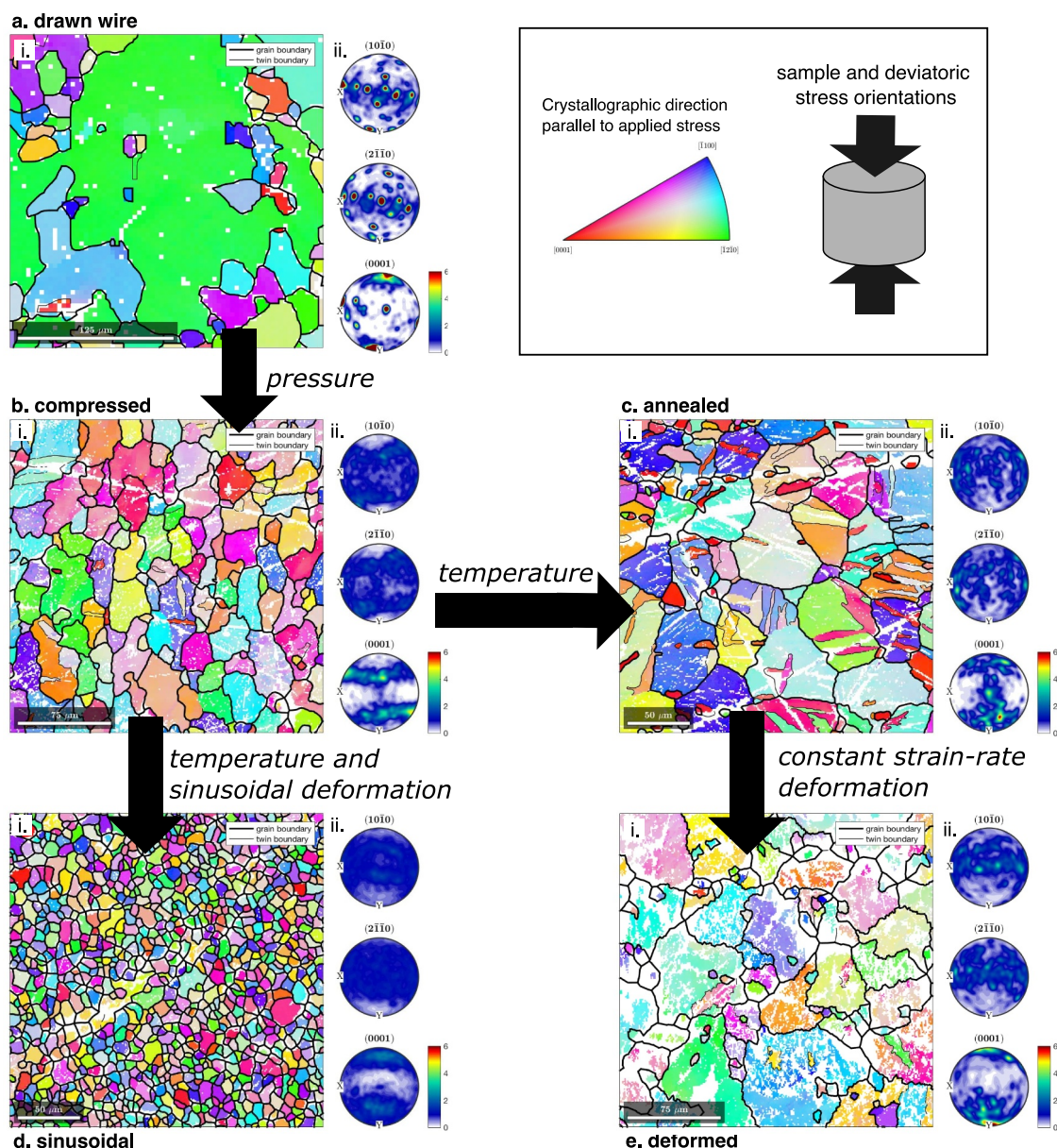


Figure 5. EBSD analysis of the samples, showing the grain and fabric evolution in the wire samples; the equivalent plots for the powder samples are in Figure S4 of the Supporting Information S1. Part (a) drawn wire, (b) after compression, (c) after annealing, (d) after sinusoidal deformation at elevated temperatures and after deformation. Parts i are EBSD maps colored by orientation and parts ii are 1-point per pixel, antipodal pole figures all plotted on the same multiples of uniform distribution color scale. White areas in the EBSD maps are where the sample was not indexed or data removed from the analysis; the linear white features in (b) and (c) are scratches. The sample cylinder axis and applied strain are vertical in the figure (d and e). For details of the compression, annealing and deformation experiments see Texts S3 and S4 in Supporting Information S1.

Significant changes between the initial and sinusoidal microstructures occur in both the wire (Figures 5 and 6, Figure S1 in Supporting Information S1) and powder samples (Text S2, Figures S4–S6 in Supporting Information S1). Sinusoidal deformation of the wire sample results in a microstructure which has a median grain-size an order of magnitude smaller than the initial, compressed, annealed or deformed samples (Figures 5d and 6a, Table 1). Sinusoidal deformation of the powder sample results in a significant increase in grain-size (Figures S4 and S6 in Supporting Information S1) and a final microstructure that is remarkably similar to that of the wire. The sinusoidally deformed samples also have weaker crystallographic preferred orientation than all other states of deformation (Figure 5dii, Figure S4dii in Supporting Information S1). There is a close correlation between the nearest-neighbor and random-pair misorientation distributions in both sinusoidally deformed samples (Figure 6c,

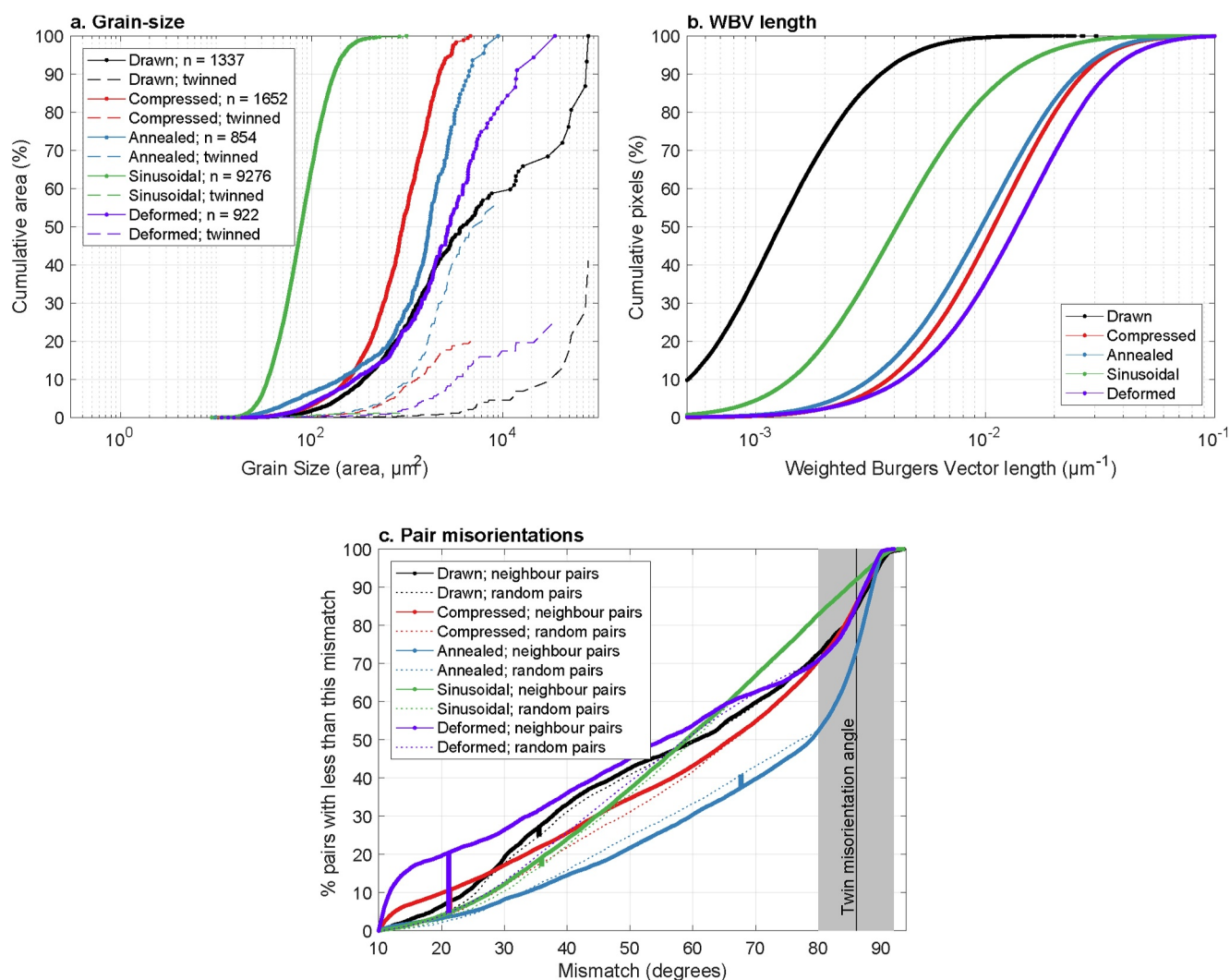


Figure 6. Cumulative distributions of wire sample microstructure: (a) Grain size, (b) weighted Burgers vector length and (c) neighbor-pair misorientation distributions; the equivalent plots for the powder samples are in Figure S6 of the Supporting Information S1. In each figure the points correspond to individual observations, where these lines appear thick the data density obscures the individual points. The dashed lines in (a), are the area of the sample that contains twinned grains. The dashed lines in (c) are the random pair misorientation distributions for the data, the thick bars show the position and size of the largest deviation of the neighbor-pair distribution from that of the random-pair distribution. The solid black lines in (c) show zinc's twin misorientation angle and the gray bar highlights the region influenced by twinning. A summary of the data here is presented in Table 1. For details of the compression, annealing and deformation experiments see Texts S3 and S4 in Supporting Information S1.

Figure S6c in Supporting Information S1) which is indicative of little or no retained crystallographic relationship between neighboring grains. This and the significant changes in grain-size indicate that the majority, if not all, of both samples has recrystallized. Extensive recrystallization in the samples is further supported by diffraction from the zinc, which above 200°C is rapid (Section 2.3, Text S4 in Supporting Information S1). The recovered sinusoidal grain-size is also more homogeneous, with fewer large or small grains, than in the other samples. There are a small number of quadruple-grain junctions between the approximately equant grains which is consistent with grain boundary sliding. The weighted Burger's vector length (WBV) in this sample is unevenly distributed; some grains have uniformly low WBV, whilst others have distinctly higher WBV (Figures S1d and S5d in Supporting Information S1). These microstructures contain all the features commonly observed in superplastically deformed alloys, namely: equiaxial grains; a low occurrence of low-angle grain boundaries; evidence of grain-boundary sliding (e.g., quadruple-grain junctions) and large fraction of recrystallized grains (Liu et al., 2012; Myshlyayev et al., 2022; Nuttall & Nicholson, 1968; Zou et al., 2024).

This contrasts with the microstructures of the compression, annealed and deformed samples (Figures 5 and 6, Figures S4 and S6 in Supporting Information S1). The grain-size of these samples is highly variable and they contain higher WBVI values that form distinct planar regions within grains indicative of subgrain boundaries (Figure S1 in Supporting Information S1). The compressed and deformed samples also have excess low angle neighbor-pair misorientations consistent with dislocations accumulating into sub-grain walls and ultimately, high-angle grain-boundaries. In addition, distinct twins were recognized with the grains and the twin plane identified as $\{10\bar{1}2\}$, consistent with previous observations (e.g., Kanitpanyacharoen et al., 2012; Liu et al., 2020). Overall our deformed samples' microstructure (Table 1) is consistent with other constant strain-rate deformation experiments (e.g., Bergman et al., 2018) and dislocation creep plus “*continuous dynamic recrystallization*” as the dominant deformation mechanism (Gourdet & Montheillet, 2003; Montheillet & Jonas, 2003).

The microstructures (Figure 5) themselves contain no evidence on the speed of their reconstruction. A rapid transformation of the microstructure is implied by (a) the absence of a transient in amplitude during the sinusoidal deformation and (b) the rapid changes in microstructure following increases in strain-rate or temperature during the stepped strain-rate experiment (Text S4 in Supporting Information S1). The rapid response of the microstructure to applied conditions coupled with the comparable microstructures in the wire and powder sinusoidal samples implies the formation of a quasi-equilibrium grain-size and an important role for grain-boundary sliding in the dissipation mechanism.

4. Discussion

This study has measured the response of zinc wire and zinc powder samples to small amplitude, axial, sinusoidal deformation. Although sinusoidal compression experiments are not able to observe superplasticity in the normal sense (i.e., hyper-extension of the sample before failure) the observations are all consistent with a superplastic deformation mechanism and a steady-state grain-size during sinusoidal deformation. In the absence of sinusoidal deformation the samples deform by dislocation creep.

The strains in the sample and standard (typically $\sim 6 \times 10^{-4}$ and $\sim 10^{-4}$ respectively) were kept as small as possible while still being resolvable with the available experimental setup. The maximum axial strain under which the response of zinc to sinusoidal strain is linear has not been measured here but under pure shear is approximately 5×10^{-5} (Burdett & Wendler, 1976). The strains here are also large compared to the strains used in previous low-pressure anelastic measurements (2×10^{-6} – 2×10^{-5} , e.g., Jackson et al., 2000). Axial stresses inferred from the corundum strain (22–84 MPa) are significantly larger than the 0.3 MPa maximum shear stress of Jackson et al. (2000). It is therefore possible that the samples are not in the linear anelastic regime, and would have an amplitude dependent response to strain.

It is generally assumed that for viscoelastic models (e.g., Burgers model) to be physically meaningful the microstructure must be constant. Instead, here the sinusoidal deformation completely reforms the microstructures (Figures 5 and 6, Figures S4 and S6 in Supporting Information S1), which transform from initial diversity to a superplastic-style microstructure (e.g., Liu et al., 2012; Myshlyayev et al., 2022; Nuttall & Nicholson, 1968; Zou et al., 2024). This is in contrast to the non-sinusoidal samples and other studies (e.g., Bergman et al., 2018) in which the samples retain elements of their original microstructure. The recovered microstructures and lack of well resolved differences in the Burgers models points toward the sample histories (i.e., wire vs. powder) not having substantial effects on the dissipation. Instead, under sinusoidal deformation, the microstructure is dominated by the experimental conditions and overwrites the preceding history.

The change in microstructure does not though preclude the validity of the Burgers model. The strong correspondence between the values of E_M and previous elastic measurements (Figure 4) supports the reasonableness of the Burgers model. The creep activation energy (η_M , 6.8 ± 1.1 and 4.2 ± 2.0 kJ/mol for the wire and powder respectively) is significantly smaller than previously measured values for steady-state creep. However, these values can be explained by a combination of “*internal stress superplasticity*,” grain-boundary sliding and a temperature dependent steady-state grain-size.

4.1. Internal Stress Superplasticity

Superplasticity is a phenomenon in which metals and ceramics undergo hyper-extension in tensile tests (Sherby & Wadsworth, 1985). “*Internal stress superplasticity*” is a particular form of superplasticity in which composites

and *hcp*-metals with sufficient anisotropy exhibit superplasticity in response to thermal cycling (~50 K amplitude; Kitazono, Hirasaka, et al., 1999; Kitazono et al., 2001; Lobb et al., 1972; Pickard & Derby, 1991; Roth et al., 1974; Schuh & Dunand, 2002; Wu et al., 1987). Internal stress superplasticity is further subclassified according to the origin of the internal stresses: *transformational superplasticity* is caused by phase transitions; *Coefficient of Thermal Expansion (CTE)-mismatch superplasticity* by anisotropic thermal expansion of a single phase and *Composite CTE-mismatch superplasticity* by differential thermal expansion of multi-phase assemblages (Kitazono et al., 1999b). Models of internal stress superplasticity postulate a “diffusion-controlled dislocation-creep deformation mechanism” that incorporates the effects of anisotropic internal stress on the motion of dislocations: promoting dislocation movement in some grains/directions and inhibiting it in others (Wu & Sherby, 1984). The effects of internal stress superplasticity in the deformation mechanism are reduced but not eliminated when the grain-size is a significant fraction of the sample volume (Pickard & Derby, 1991). Overall though, internal stress superplasticity is not well understood, the literature is not extensive and the theory is incomplete.

Nevertheless, consistent with the observations here, internal stress superplasticity has a lower activation energy for creep (Schuh & Dunand, 2002). This is explained in conceptual models by the activation energy containing a factor of $1/n$, where n is the stress exponent for dislocation creep. In zinc, $n \geq 4$ which will reduce the activation energies from those for dislocation-mitigated creep mechanisms but this factor alone is not enough to match our activation energy with previous measurements.

However, here we also observe reformation of the microstructure which points to additional factors that can also reduce the measured activation energy. The uniform and converged grain-sizes in the sinusoidal samples (Figure 5, Figure S4 in Supporting Information S1) and the rapid-grain growth in the annealed and deformed samples combine to imply that the sinusoidal deformation prevents grain-growth above a critical size and that sliding along grain-boundaries is an important part of the dissipation mechanism. Grains that are larger than this critical size experience increases in internal stress that are sufficient to trigger grain-size reduction. Grain-size reduction occurs by dislocations accumulating into sub-grain boundaries and then into new grains, consistent with theories of internal stress superplasticity. Grain-boundary sliding reorganizes these new grains, removing any excess low-angle misorientation pairs; just as is observed here in the sinusoidal microstructures (Figure 6c and Figure S6c in Supporting Information S1). Interface energy provides an opposite driving force to increase average grain size, by the elimination of small grains. Thus, competition between internal-stresses and interface energy, coupled with grain-boundary sliding, results in a uniform, steady-state grain-size that is determined by the relative strength of driving forces. The relative strength of the driving forces is determined by the temperature and the amplitude of the applied sinusoidal strain. Changes in either of these will alter the balance of force and therefore the steady-state grain-size. Higher temperatures increase the relative interface energy and therefore the steady-state grain-size.

Larger grain-sizes have slower deformation rates when deforming by grain-boundary sliding (e.g., Korla & Chokshi, 2014) and/or diffusion creep (Raj & Ashby, 1971). Deformation at higher temperatures, with a larger grain-size, is therefore slower than would be expected for a constant grain-size. An increase in grain-size with temperature therefore results in a smaller apparent activation energy. Here the temperature dependent steady-state grain-size that therefore results in an activation energy that is smaller than the activation energy for the physical processes active in the sample (Table 4). We therefore conclude that a combination of internal stress superplasticity, grain-boundary sliding and a steady-state grain-size are responsible for the very low activation energies of η_M .

Moreover, the small range of $Q^{-1}(\omega)$ in both the wire and the powder samples (Table 3) is consistent with a varying grain-size which focuses the dissipation peak in the parameter space of the data. This agrees with previous studies that showed superplastic metals have enhanced dissipation relative to their non-superplastic form (Martínez-Flores et al., 2009; Park et al., 2002).

These conclusions are only valid though if internal stress superplasticity is activated within the zinc samples. Internal stress superplastic is activated when the internally generated stresses are larger than the externally applied stress but it has not previously been reported in mechanically oscillating conditions. The magnitude of anisotropy is a crucial factor in the development of internal stresses. Coefficient of Thermal Expansion-mismatch superplasticity has previously been observed in zinc (Roth et al., 1974; Wu et al., 1987) and depends on significant anisotropy of thermal expansion to generate internal stress. In zinc, the thermal expansion is ~5.0 times larger in

the $\langle 11\bar{2}0 \rangle$ (or a) than the [0001] (or c) crystallographic direction (Nuss et al., 2010). In the thermal cycling regime (± 50 K), the expected axial strains are $\epsilon_a \sim 0.0012$ and $\epsilon_c \sim 0.0062$. For mechanical strain, the axial compressibilities are the equivalent physical property; the ratio of which in zinc is ~ 3.2 . Under the conditions of these experiments ($\pm \sim 54$ MPa) strains of $\epsilon_a \sim 0.0007$, $\epsilon_c \sim 0.0022$ are expected. The equivalence of thermal expansion and compressibility are further supported by observations of significant internal stresses generated during both compression (Davidson et al., 1965; Gelles, 1966) and cooling of zinc (Leineweber et al., 2009).

Although the strains here are smaller than in the thermal cycling experiments, the reformed microstructure together with the small activation energy, strongly indicates that (athermal) small strain sinusoidal deformation has activated internal stress superplastic deformation in our samples. This previously unrecognized form of internal stress superplasticity generates internal stress due to the anisotropic compressibility of a single phase which we name here as “*elastic strain mismatch superplasticity*.” Thus it is comparable to, but distinct from, the preceding three types of internal stress superplasticity, namely: transformational-, Coefficient of Thermal Expansion mismatch- and Composite CTE-mismatch-superplasticity (Kitazono et al., 1999b).

4.2. Inner Core Dissipation

This study and *Elastic strain mismatch superplasticity* have consequences for our understanding of the Earth's inner-core. The observations here contrast with previous arguments that *hcp* metals are “*quite elastic*” (e.g., Belonoshko et al., 2019). Instead, the results show that *hcp*-zinc samples exhibit significant deviations from purely elastic behavior and have similar magnitude of dissipation to that observed in *bcc* and *fcc*-iron (Jackson et al., 2000).

Most *hcp*-metals, including *hcp*-iron, are though less anisotropic than zinc (e.g., Takemura, 2019; Tromans, 2011) and it is not known how ubiquitous internal stress superplasticity is in *hcp*-metals. But at the homologous temperatures of the inner-core ($T/T_m \lesssim 1$) dynamic recrystallization will be extremely rapid. The inner-core will therefore respond quickly to even small changes in stress, making internal stress superplasticity in the inner-core conceivable. When it does occur, the magnitude of any superplastic response will depend on the anisotropy and how quickly the material recrystallizes in response to stress.

Assuming that this phenomena does occur in *hcp*-iron and the Earth's inner-core, even the smallest estimates of inner-core grain-size (e.g., Bergman, 1998) are significantly larger than is present in our experiments. However, Pickard and Derby (1991) showed that the effects of internal stress superplasticity are reduced but not eliminated when the grain-size approaches that of the sample volume; this reduction will also decrease, but not eliminate, the associated dissipation. Therefore as long as the grain-size is less than the wave length of the seismic waves (c. 1–10 km) internal stress superplasticity could act to dissipate the seismic waves. Changes in inner core Q^{-1} (Doornbos, 1974; Li & Cormier, 2002; Pejić et al., 2019; Suda & Fukao, 1990) could therefore reflect the spatial variability of grain-size and/or grain-orientation, which will control the impact of internal stress superplasticity mechanisms on seismic attenuation.

5. Conclusions

The high-pressure response of zinc wire to sinusoidal stress at seismic frequencies and up to $T/T_m \sim 0.8$ have been measured and show that the *hcp* metal zinc has significant dissipation at seismic frequencies. The experiments show that significant dissipation occurs without the need for a fluid phase or significant impurities; instead the strain is accommodated by *elastic strain mismatch superplasticity*. This is a form of internal stress superplasticity controlled by anisotropic compressibility in the sample.

The micromechanical data are best reproduced by a simple Burgers model (Equation 5). The elastic components of the model (E_M) show a good correspondence to previous studies (Figure 4). The activation energy for creep (E_{a,η_M}) is much lower than previous studies have found but is consistent with an activation energy for internal stress superplasticity combined with a varying grain-size. The values of E_V and η_V are less well constrained and do not simply correspond to a distinct physical process. It is therefore probable that the Burgers model is too simplistic to properly describe the dissipative processes active in the sample but there is not sufficient data to warrant the use of more complex models. Nevertheless, the experiments here show that significant viscoelastic softening occurs at high pressure and temperature in zinc.

The grain size is inferred to change throughout the experiments in response to the temperature and mechanical cycling conditions, which overwrites the initial fabric leading to the convergence of grain size and WBVI in initially very different samples. This contrasts with complimentary constant strain-rate deformation experiments under similar conditions which deform by dislocation creep and in which the samples retain hall marks of the original microstructure. The switch in deformation mechanism is consistent with thermal cycling experiments in which the constantly varying stress induces a change in deformation mechanism from dislocation creep to “Coefficient of thermal expansion-mismatch superplasticity.”

With internal stress superplasticity, the internal stresses are large compared to the applied stress. It is active under cyclic conditions and changes the deformation mechanisms even when the grain size is a substantial fraction of the gauge volume (Pickard & Derby, 1991). Anisotropic compressibility is a feature of *hcp* metals and it is therefore possible that *hcp*-Fe will also exhibit internal stress superplasticity under sinusoidal straining. Where active in the inner-core, internal stress superplasticity limits the maximum possible grain-size to <1–10 km and may explain regional variations in Q^{-1} by changes in grain-size. More work is needed in order to fully understand this deformation mechanism and its application to the inner-core, but it should be considered when interpreting the inner core's seismic velocity structure.

Data Availability Statement

The data collected in the course of this study are available from <https://www.bgs.ac.uk/discoverymetadata/13607352.html>.

Acknowledgments

S.A.H. (NE/H016309, NE/L006898, NE/P017525), A.M.W. (NE/K008803/1 and NE/M000044/1), S.S. (NE/K006290/1), and O.T.L. (NE/J018945/1) thank the Natural Environment Research Council (NERC) for funding. Use of the National Synchrotron Light Source (NSLS), Brookhaven National Laboratory, was supported by the U.S. Department of Energy, Office of Science, Office of Basic Energy Sciences, under Contract No. DE-AC02-98CH10886. Use of the X17B2 beamline was supported by COMPRES, the Consortium for Materials Properties Research in Earth Sciences under NSF Cooperative Agreement EAR 10-43050 and by the Mineral Physics Institute, Stony Brook University. The authors thank Diamond Light Source for providing beamtime (proposal number MG23970-1) and I12 beamline staff for technical assistance. Finally, we would like to thank Dr Richard Walshaw for his efforts in recommissioning the electron optics facility at Leeds and collecting the last few EBSD data sets under challenging conditions during the pandemic of 2020/21.

References

- Alers, G., & Neighbours, J. (1958). The elastic constants of zinc between 4.2° and 670°K. *Journal of Physics and Chemistry of Solids*, 7(1), 58–64. [https://doi.org/10.1016/0022-3697\(58\)90180-x](https://doi.org/10.1016/0022-3697(58)90180-x)
- Aning, A., Suzuki, T., & Wuttig, M. (1982). Nonlinear anelasticity of magnesium. *Journal of Applied Physics*, 53(10), 6797–6808. <https://doi.org/10.1063/1.330068>
- Antonangeli, D., Morard, G., Paolasini, L., Garbarino, G., Murphy, C. A., Edmund, E., et al. (2018). Sound velocities and density measurements of solid *hcp*-Fe and *hcp*-Fe-Si (9 wt.%) alloy at high pressure: Constraints on the Si abundance in the Earth's inner core. *Earth and Planetary Science Letters*, 482, 446–453. <https://doi.org/10.1016/j.epsl.2017.11.043>
- Antonangeli, D., Siebert, J., Badro, J., Farber, D. L., Fiquet, G., Morard, G., & Ryerson, F. J. (2010). Composition of the Earth's inner core from high-pressure sound velocity measurements in Fe-Ni-Si alloys. *Earth and Planetary Science Letters*, 295(1–2), 292–296. <https://doi.org/10.1016/j.epsl.2010.04.018>
- Aubert, J., Amit, H., Hulot, G., & Olson, P. (2008). Thermochemical flows couple the Earth's inner core growth to mantle heterogeneity. *Nature*, 454(7205), 758–761. <https://doi.org/10.1038/nature07109>
- Bachmann, F., Hielscher, R., & Schaeben, H. (2010). Texture analysis with MTEX—free and open source software toolbox. *Solid State Phenomena*, 160, 63–68. <https://doi.org/10.4028/www.scientific.net/SSP.160.63>
- Bachmann, F., Hielscher, R., & Schaeben, H. (2011). Grain detection from 2D and 3D EBSD data—Specification of the MTEX algorithm. *Ultramicroscopy*, 111(12), 1720–1733. <https://doi.org/10.1016/j.ultramic.2011.08.002>
- Banks, H. T., Hu, S., & Kenz, Z. R. (2011). A brief review of elasticity and viscoelasticity for solids. *Advances in Applied Mathematics and Mechanics*, 3, 1–51. <https://doi.org/10.4208/aamm.10-m1030>
- Bazhanova, Z. G., Roizen, V. V., & Oganov, A. R. (2017). High-pressure behavior of the Fe-S system and composition of the Earth's inner core. *Physics-Uspekhi*, 60(10), 1025–1032. <https://doi.org/10.3367/ufne.2017.03.038079>
- Belonoshko, A. B., Fu, J., Bryk, T., Simak, S. I., & Mattesini, M. (2019). Low viscosity of the Earth's inner core. *Nature Communications*, 10(1), 2483. <https://doi.org/10.1038/s41467-019-10346-2>
- Bergman, M. I. (1998). Estimates of the Earth's inner core grain size. *Geophysical Research Letters*, 25(10), 1593–1596. <https://doi.org/10.1029/98GL01239>
- Bergman, M. I., Yu, J., Lewis, D. J., & Parker, G. K. (2018). Grain boundary sliding in high-temperature deformation of directionally solidified *hcp* Zn alloys and implications for the deformation mechanism of Earth's inner core. *Journal of Geophysical Research: Solid Earth*, 123(1), 189–203. <https://doi.org/10.1002/2017JB014881>
- Burdett, C. F., & Wendler, B. (1976). On the background damping in the vicinity of the grain-boundary damping peak in zinc. *Journal of Materials Science*, 11(5), 817–822. <https://doi.org/10.1007/BF00542296>
- Cao, A., & Romanowicz, B. (2004). Hemispherical transition of seismic attenuation at the top of the Earth's inner core. *Earth and Planetary Science Letters*, 228(3–4), 243–253. <https://doi.org/10.1016/j.epsl.2004.09.032>
- Caracas, R. (2015). The influence of hydrogen on the seismic properties of solid iron. *Geophysical Research Letters*, 42(10), 3780–3785. <https://doi.org/10.1002/2015gl063478>
- Chabildas, L. C., & Gilder, H. M. (1972). Thermal coefficient of expansion of an activated vacancy in zinc from high-pressure self-diffusion experiments. *Physical Review B*, 5(6), 2135–2144. <https://doi.org/10.1103/physrevb.5.2135>
- Cooper, R., & Washburn, J. (1967). Stress-induced movement of twin boundaries in zinc. *Acta Metallurgica*, 15(4), 639–647. [https://doi.org/10.1016/0001-6160\(67\)90107-1](https://doi.org/10.1016/0001-6160(67)90107-1)
- Cooper, R. F. (2002). Seismic wave attenuation: Energy dissipation in viscoelastic crystalline solids. *Reviews in Mineralogy and Geochemistry*, 51(1), 253–290. <https://doi.org/10.2138/gsrng.51.1.253>
- Cottrell, A. H., & Aytakin, V. (1947). Andrade's creep law and the flow of zinc crystals. *Nature*, 160(4062), 328–329. <https://doi.org/10.1038/160328a0>

- Davidson, T. E., Uy, J. C., & Lee, A. P. (1965). Hydrostatic pressure-induced plastic flow in polycrystalline metals. *Transactions of the Metallurgical Society of AIME*, 233, 820–826.
- Deuss, A. (2014). Heterogeneity and anisotropy of Earth's inner core. *Annual Review of Earth and Planetary Sciences*, 42(1), 103–126. <https://doi.org/10.1146/annurev-Earth-060313-054658>
- Dobson, D. P., Hunt, S. A., Li, L., & Weidner, D. J. (2008). Measurement of thermal diffusivity at high pressures and temperatures using synchrotron radiography. *Mineralogical Magazine*, 72(2), 653–658. <https://doi.org/10.1180/minmag.2008.072.2.653>
- Dobson, D. P., Hunt, S. A., McCormack, R., Lord, O. T., Weidner, D. J., Li, L., & Walker, A. M. (2010). Thermal diffusivity of MORB-composition rocks to 15 GPa: Implications for triggering of deep seismicity. *High Pressure Research*, 30(3), 406–414. <https://doi.org/10.1080/08957959.2010.516827>
- Dobson, D. P., McCormack, R., Hunt, S. A., Ammann, M. W., Weidner, D., Li, L., & Wang, L. (2012b). The relative strength of perovskite and post-perovskite NaCoF₃. *Mineralogical Magazine*, 76(4), 925–932. <https://doi.org/10.1180/minmag.2012.076.4.09>
- Doornbos, D. J. (1974). The anelasticity of the inner core. *Geophysical Journal International*, 38(2), 397–415. <https://doi.org/10.1111/j.1365-246x.1974.tb04131.x>
- Durham, W. B., Weidner, D. J., Karato, S. I., & Wang, Y. B. (2002). New developments in deformation experiments at high pressure. In S. Karato, & H. Wenk (Eds.), *Plastic deformation of minerals and rocks, reviews in mineralogy & geochemistry* (Vol. 51, pp. 21–49). Mineralogical Society of America. <https://doi.org/10.2138/gsrmg.51.1.21>
- Faul, U., & Jackson, I. (2015). Transient creep and strain energy dissipation: An experimental perspective. *Annual Review of Earth and Planetary Sciences*, 43(1), 541–569. <https://doi.org/10.1146/annurev-Earth-060313-054732>
- Fearn, D. R., Loper, D. E., & Roberts, P. H. (1981). Structure of the Earth's inner core. *Nature*, 292(5820), 232–233. <https://doi.org/10.1038/292232a0>
- Fei, Y. (1995). Thermal expansion. In *AGU reference shelf* (pp. 29–44). American Geophysical Union. <https://doi.org/10.1029/rf002p0029>
- Fei, Y., Murphy, C., Shibasaki, Y., Shahar, A., & Huang, H. (2016). Thermal equation of state of hcp-iron: Constraint on the density deficit of Earth's solid inner core. *Geophysical Research Letters*, 43(13), 6837–6843. <https://doi.org/10.1002/2016gl069456>
- Fiquet, G., Badro, J., Guyot, F., Requardt, H., & Krisch, M. (2001). Sound velocities in iron to 110 Gigapascals. *Science*, 291(5503), 468–471. <https://doi.org/10.1126/science.291.5503.468>
- Gelles, S. H. (1966). Hydrostatic pressure-induced deformation of polycrystalline zinc. *Transactions of the Metallurgical Society of AIME*, 236, 981–987.
- Gieske, J. H., & Barsch, G. R. (1968). Pressure dependence of the elastic constants of single crystalline aluminum oxide. *Physica Status Solidi (b)*, 29(1), 121–131. <https://doi.org/10.1002/pssb.19680290113>
- Goto, T., Anderson, O. L., Ohno, I., & Yamamoto, S. (1989). Elastic constants of corundum up to 1825 K. *Journal of Geophysical Research*, 94(B6), 7588–7602. <https://doi.org/10.1029/jb094ib06p07588>
- Gourdet, S., & Montheillet, F. (2003). A model of continuous dynamic recrystallization. *Acta Materialia*, 51(9), 2685–2699. [https://doi.org/10.1016/S1359-6454\(03\)00078-8](https://doi.org/10.1016/S1359-6454(03)00078-8)
- Gribb, T. T., & Cooper, R. F. (1998). Low-frequency shear attenuation in polycrystalline olivine: Grain boundary diffusion and the physical significance of the Andrade model for viscoelastic rheology. *Journal of Geophysical Research*, 103(B11), 27267–27279. <https://doi.org/10.1029/98jb02786>
- Hunt, S. A. (2023). *FoilTrack*: A package to increase strain-resolution by improved X-radiographic image processing. *High Pressure Research*, 43(4), 1–16. <https://doi.org/10.1080/08957959.2023.2247542>
- Hunt, S. A., Davies, D. R., Walker, A. M., McCormack, R. J., Wills, A. S., Dobson, D. P., & Li, L. (2012). On the increase in thermal diffusivity caused by the perovskite to post-perovskite phase transition and its implications for mantle dynamics. *Earth and Planetary Science Letters*, 319(320), 96–103. <https://doi.org/10.1016/j.epsl.2011.12.009>
- Hunt, S. A., Dobson, D. P., Li, L., Weidner, D. J., & Brodholt, J. P. (2010). Relative strength of the pyrope-majorite solid solution and the flow-law of majorite containing garnets. *Physics of the Earth and Planetary Interiors*, 179(1–2), 87–95. <https://doi.org/10.1016/j.pepi.2009.12.001>
- Hunt, S. A., Walker, A. M., McCormack, R., Dobson, D. P., Wills, A. S., & Li, L. (2011). The effect of pressure on thermal diffusivity in pyroxenes. *Mineralogical Magazine*, 75(5), 2597–2610. <https://doi.org/10.1180/minmag.2011.075.5.2597>
- Hunt, S. A., Weidner, D. J., Li, L., Wang, L., Walte, N. P., Brodholt, J. P., & Dobson, D. P. (2009). Weakening of calcium iridate during its transformation from perovskite to post-perovskite. *Nature Geoscience*, 2(11), 794–797. <https://doi.org/10.1038/ngeo663>
- Hunt, S. A., Whitaker, M. L., Bailey, E., Mariani, E., Stan, C. V., & Dobson, D. P. (2019). An experimental investigation of the relative strength of the silica polymorphs quartz, coesite, and stishovite. *Geochemistry, Geophysics, Geosystems*, 20(4), 1975–1989. <https://doi.org/10.1029/2018GC007842>
- Irving, J. C., & Deuss, A. (2011). Stratified anisotropic structure at the top of Earth's inner core: A normal mode study. *Physics of the Earth and Planetary Interiors*, 186(1–2), 59–69. <https://doi.org/10.1016/j.pepi.2011.03.003>
- Jackson, I. (2015). Properties of rocks and minerals: Physical origins of anelasticity and attenuation in rock. In *Treatise on geophysics* (pp. 539–571). Elsevier. <https://doi.org/10.1016/b978-0-444-53802-4.00045-2>
- Jackson, I., Gerald, J. D. F., & Kokkonen, H. (2000). High-temperature viscoelastic relaxation in iron and its implications for the shear modulus and attenuation of the Earth's inner core. *Journal of Geophysical Research*, 105(B10), 23605–23634. <https://doi.org/10.1029/2000jb900131>
- Kanitpanyacharoen, W., Merkel, S., Miyagi, L., Kaercher, P., Tomé, C., Wang, Y., & Wenk, H.-R. (2012). Significance of mechanical twinning in hexagonal metals at high pressure. *Acta Materialia*, 60(1), 430–442. <https://doi.org/10.1016/j.actamat.2011.07.055>
- Kitazono, K., Hirasaka, R., Sato, E., Kuribayashi, K., & Motegi, T. (1999). Effects of crystallographic texture on internal stress superplasticity induced by anisotropic thermal expansion. *MRS Proceedings*, 601, 199. <https://doi.org/10.1557/PROC-601-199>
- Kitazono, K., Hirasaka, R., Sato, E., Kuribayashi, K., & Motegi, T. (2001). Internal stress superplasticity in anisotropic polycrystalline materials. *Acta Materialia*, 49(3), 473–486. [https://doi.org/10.1016/S1359-6454\(00\)00336-0](https://doi.org/10.1016/S1359-6454(00)00336-0)
- Kitazono, K., Sato, E., & Kuribayashi, K. (1999). Unified interpretation of internal stress superplasticity models based on thermally-activated kinetics. *Acta Materialia*, 47(5), 1653–1660. [https://doi.org/10.1016/S1359-6454\(98\)00431-5](https://doi.org/10.1016/S1359-6454(98)00431-5)
- Korla, R., & Chokshi, A. H. (2014). A constitutive equation for grain boundary sliding: An experimental approach. *Metallurgical and Materials Transactions A*, 45(2), 698–708. <https://doi.org/10.1007/s11661-013-2017-z>
- Lakes, R. S. (1999). *Viscoelastic solids*. CRC Press.
- Ledbetter, H. M. (1977). Elastic properties of zinc: A compilation and a review. *Journal of Physical and Chemical Reference Data*, 6(4), 1181–1203. <https://doi.org/10.1063/1.555564>
- Leineweber, A., Mittermeijer, E. J., Lawson, A. C., Roberts, J. A., Valdez, J. A., & Kreher, W. S. (2009). Thermally induced microstrain broadening in polycrystalline hexagonal zinc. *Zeitschrift für Kristallographie Supplements*, 2009(30), 97–102. <https://doi.org/10.1524/zksu.2009.0014>

- Li, D., & Wagoner, R. H. (2021). The nature of yielding and anelasticity in metals. *Acta Materialia*, 206, 116625. <https://doi.org/10.1016/j.actamat.2021.116625>
- Li, L., & Weidner, D. J. (2007). Energy dissipation of materials at high pressure and high temperature. *Review of Scientific Instruments*, 78(5), 053902. <https://doi.org/10.1063/1.2735587>
- Li, X., & Cormier, V. F. (2002). Frequency-dependent seismic attenuation in the inner core, 1. A viscoelastic interpretation. *Journal of Geophysical Research*, 107(B12), ESE13–1–ESE13–20. <https://doi.org/10.1029/2002jb001795>
- Li, Y., Vočadlo, L., & Brodholt, J. P. (2018). The elastic properties of hcp-Fe alloys under the conditions of the Earth's inner core. *Earth and Planetary Science Letters*, 493, 118–127. <https://doi.org/10.1016/j.epsl.2018.04.013>
- Liu, F., Xue, P., & Ma, Z. (2012). Microstructural evolution in recrystallized and unrecrystallized Al–Mg–Sc alloys during superplastic deformation. *Materials Science and Engineering: A*, 547, 55–63. <https://doi.org/10.1016/j.msea.2012.03.076>
- Liu, S., Kent, D., Zhan, H., Doan, N., Dargusch, M., & Wang, G. (2020). Dynamic recrystallization of pure zinc during high strain-rate compression at ambient temperature. *Materials Science and Engineering: A*, 784, 139325. <https://doi.org/10.1016/j.msea.2020.139325>
- Lloyd, G. E. (1987). Atomic number and crystallographic contrast images with the SEM: A review of backscattered electron techniques. *Mineralogical Magazine*, 51(359), 3–19. <https://doi.org/10.1180/minmag.1987.051.359.02>
- Lobb, R. C., Sykes, E. C., & Johnson, R. H. (1972). The superplastic behaviour of anisotropic metals thermally cycled under stress. *Metal Science Journal*, 6(1), 33–39. <https://doi.org/10.1179/030634572790445876>
- Lythgoe, K., Deuss, A., Rudge, J., & Neufeld, J. (2014). Earth's inner core: Innermost inner core or hemispherical variations? *Earth and Planetary Science Letters*, 385, 181–189. <https://doi.org/10.1016/j.epsl.2013.10.049>
- Mäkinen, A. M., Deuss, A., & Redfern, S. A. T. (2014). Anisotropy of Earth's inner core intrinsic attenuation from seismic normal mode models. *Earth and Planetary Science Letters*, 404, 354–364. <https://doi.org/10.1016/j.epsl.2014.08.009>
- Mao, Z., Lin, J.-F., Liu, J., Alatas, A., Gao, L., Zhao, J., & Mao, H.-K. (2012). Sound velocities of Fe and Fe-Si alloy in the Earth's core. *Proceedings of the National Academy of Sciences of the United States of America*, 109(26), 10239–10244. <https://doi.org/10.1073/pnas.1207086109>
- Martínez-Flores, E. E., Negrete, J., & Torres-Villaseñor, G. (2009). Relationship between loss-modulus and homologous temperature in superplastic alloys. *Journal of Thermal Analysis and Calorimetry*, 97(3), 891–894. <https://doi.org/10.1007/s10973-009-0163-8>
- Matsunaga, T., Kameyama, T., Ueda, S., & Sato, E. (2010). Grain boundary sliding during ambient-temperature creep in hexagonal close-packed metals. *Philosophical Magazine*, 90(30), 4041–4054. <https://doi.org/10.1080/14786435.2010.502883>
- Merkel, S., Wenk, H.-R., Gillet, P., Mao, H. K., & Hemley, R. J. (2004). Deformation of polycrystalline iron up to 30 GPa and 1000 K. *Physics of the Earth and Planetary Interiors*, 145(1–4), 239–251. <https://doi.org/10.1016/j.pepi.2004.04.001>
- Montheillet, F., & Jonas, J. J. (2003). *Recrystallization, dynamic* (pp. 205–225). John Wiley & Sons, Ltd. <https://doi.org/10.1002/3527600434.eap388>
- Murthy, G. S., & Sastry, D. H. (1982). Impression creep of zinc and the rate-controlling dislocation mechanism of plastic flow at high temperatures. *Physica Status Solidi*, 70(1), 63–71. <https://doi.org/10.1002/pssa.2210700110>
- Myshlyayev, M., Mironov, S., Korznikova, G., Konkova, T., Korznikova, E., Aletdinov, A., et al. (2022). EBSD study of superplasticity: New insight into a well-known phenomenon. *Journal of Alloys and Compounds*, 898, 162949. <https://doi.org/10.1016/j.jallcom.2021.162949>
- Nishihara, Y., Doi, S., Tsujino, N., Yamazaki, D., Matsukage, K. N., Tsubokawa, Y., et al. (2023). Rheology of hexagonal close-packed (hcp) iron. *Journal of Geophysical Research: Solid Earth*, 128(6), e2022JB026165. <https://doi.org/10.1029/2022JB026165>
- Niu, F., & Wen, L. (2001). Hemispherical variations in seismic velocity at the top of the Earth's inner core. *Nature*, 410(6832), 1081–1084. <https://doi.org/10.1038/35074073>
- Nowick, A. S., & Berry, B. S. (1972). *Anelastic relaxation in crystalline solids*. Academic Press.
- Nuss, J., Wedig, U., Kirfel, A., & Jansen, M. (2010). The structural anomaly of zinc: Evolution of lattice constants and parameters of thermal motion in the temperature range of 40 to 500 K. *Zeitschrift für Anorganische und Allgemeine Chemie*, 636(2), 309–313. <https://doi.org/10.1002/zaac.200900460>
- Nuttall, K., & Nicholson, R. B. (1968). Microstructure of superplastic alloys. *The Philosophical Magazine: A Journal of Theoretical Experimental and Applied Physics*, 17(149), 1087–1091. <https://doi.org/10.1080/14786436808223186>
- Park, K.-T., Kim, W.-J., & Shin, D.-H. (2002). Analysis on the anelasticity of a superplastic Zn-22% Al eutectoid. *Materials Science and Engineering: A*, 322(1–2), 159–166. [https://doi.org/10.1016/S0921-5093\(01\)01129-7](https://doi.org/10.1016/S0921-5093(01)01129-7)
- Pejić, T., Hawkins, R., Sambridge, M., & Tkalčić, H. (2019). Transdimensional Bayesian attenuation tomography of the upper inner core. *Journal of Geophysical Research: Solid Earth*, 124(2), 1929–1943. <https://doi.org/10.1029/2018jb016400>
- Pickard, S., & Derby, B. (1991). The influence of microstructure on internal stress superplasticity in polycrystalline zinc. *Scripta Metallurgica et Materialia*, 25(2), 467–472. [https://doi.org/10.1016/0956-716X\(91\)90212-J](https://doi.org/10.1016/0956-716X(91)90212-J)
- Prescher, C., Dubrovinsky, L., Bykova, E., Kuppenko, I., Glazyrin, K., Kantor, A., et al. (2015). High Poisson's ratio of Earth's inner core explained by carbon alloying. *Nature Geoscience*, 8(3), 220–223. <https://doi.org/10.1038/ngeo2370>
- Raj, R., & Ashby, M. F. (1971). On grain boundary sliding and diffusional creep. *Metallurgical Transactions A*, 2(4), 1113–1127. <https://doi.org/10.1007/BF02664244>
- Roberts, J. M., & Brown, N. (1962). Low frequency internal friction in zinc single crystals. *Acta Metallurgica*, 10(4), 430–441. [https://doi.org/10.1016/0001-6160\(62\)90022-6](https://doi.org/10.1016/0001-6160(62)90022-6)
- Roth, K., Fleck, R., & Taplin, D. (1974). The role of solutes during intergranular failure of zinc under isothermal and thermal cycling creep. *Materials Science and Engineering*, 16(3), 251–260. [https://doi.org/10.1016/0025-5416\(74\)90162-1](https://doi.org/10.1016/0025-5416(74)90162-1)
- Sakamaki, T., Ohtani, E., Fukui, H., Kamada, S., Takahashi, S., Sakairi, T., et al. (2016). Constraints on Earth's inner core composition inferred from measurements of the sound velocity of hcp-iron in extreme conditions. *Science Advances*, 2, e1500802. <https://doi.org/10.1126/sciadv.1500802>
- Schuh, C., & Dunand, D. (2002). Enhanced densification of zinc powders through thermal cycling. *Acta Materialia*, 50(6), 1349–1358. [https://doi.org/10.1016/S1359-6454\(01\)00439-6](https://doi.org/10.1016/S1359-6454(01)00439-6)
- Sherby, O. D., & Wadsworth, J. (1985). Superplasticity and superplastic forming processes. *Materials Science and Technology*, 1(11), 925–936. <https://doi.org/10.1179/mst.1985.1.11.925>
- Shirn, G., Wajda, E., & Huntington, H. (1953). Self-diffusion in zinc. *Acta Metallurgica*, 1(5), 513–518. [https://doi.org/10.1016/0001-6160\(53\)90081-9](https://doi.org/10.1016/0001-6160(53)90081-9)
- Singh, S. C., Taylor, M. A. J., & Montagner, J. P. (2000). On the presence of liquid in Earth's inner core. *Science*, 287(5462), 2471–2474. <https://doi.org/10.1126/science.287.5462.2471>
- Srinivasan, R., & Rao, R. R. (1971). Anharmonic properties of the hexagonal metals, magnesium, zinc and beryllium—I. Lattice dynamics and third order elastic constants. *Journal of Physics and Chemistry of Solids*, 32(8), 1769–1788. [https://doi.org/10.1016/s0022-3697\(71\)80143-9](https://doi.org/10.1016/s0022-3697(71)80143-9)

- Suda, N., & Fukao, Y. (1990). Structure of the inner core inferred from observations of seismic core modes. *Geophysical Journal International*, 103(2), 403–413. <https://doi.org/10.1111/j.1365-246x.1990.tb01779.x>
- Sumita, I., & Bergman, M. (2015). Inner core dynamics. In *Treatise on geophysics* (pp. 297–316). Elsevier. <https://doi.org/10.1016/b978-0-444-53802-4.00143-3>
- Sundberg, M., & Cooper, R. F. (2010). A composite viscoelastic model for incorporating grain boundary sliding and transient diffusion creep: Correlating creep and attenuation responses for materials with a fine grain size. *Philosophical Magazine*, 90(20), 2817–2840. <https://doi.org/10.1080/14786431003746656>
- Tagawa, S., Ohta, K., Hirose, K., Kato, C., & Ohishi, Y. (2016). Compression of Fe-Si-H alloys to core pressures. *Geophysical Research Letters*, 43(8), 3686–3692. <https://doi.org/10.1002/2016gl068848>
- Takahashi, S. (1952). Anelasticity of zinc. *Journal of Applied Physics*, 23(8), 866–868. <https://doi.org/10.1063/1.1702321>
- Takemura, K. (2019). The zinc story under high pressure. *Journal of Minerals and Materials Characterization and Engineering*, 07(05), 354–372. <https://doi.org/10.4236/jmmce.2019.75024>
- Tateno, S., Hirose, K., Komabayashi, T., Ozawa, H., & Ohishi, Y. (2012). The structure of Fe-Ni alloy in Earth's inner core. *Geophysical Research Letters*, 39(12), L052103. <https://doi.org/10.1029/2012GL052103>
- Tateno, S., Hirose, K., Ohishi, Y., & Tatsumi, Y. (2010). The structure of iron in Earth's inner core. *Science*, 330(6002), 359–361. <https://doi.org/10.1126/science.1194662>
- Tateno, S., Kuwayama, Y., Hirose, K., & Ohishi, Y. (2015). The structure of Fe-Si alloy in Earth's inner core. *Earth and Planetary Science Letters*, 418, 11–19. <https://doi.org/10.1016/j.epsl.2015.02.008>
- Tegart, W. J. M., & Sherby, O. D. (1958). Activation energies for high temperature creep of polycrystalline zinc. *Philosophical Magazine*, 3(35), 1287–1296. <https://doi.org/10.1080/14786435808233311>
- Thompson, D. O. (1955). Temperature dependent creep in zinc crystals. *Journal of Applied Physics*, 26(3), 280–285. <https://doi.org/10.1063/1.1721978>
- Tromans, D. (2011). Elastic anisotropy of hcp metal crystals and polycrystals. *International Journal of Research and Reviews in Applied Sciences*, 6, 462–483.
- Wajda, E. S. (1954). Grain boundary self-diffusion in zinc. *Acta Metallurgica*, 2, 184–187. [https://doi.org/10.1016/0001-6160\(54\)90157-1](https://doi.org/10.1016/0001-6160(54)90157-1)
- Walker, A. M., & Wookey, J. (2012). MSAT—A new toolkit for the analysis of elastic and seismic anisotropy. *Computers & Geosciences*, 49, 81–90. <https://doi.org/10.1016/j.cageo.2012.05.031>
- Wang, Y., Durham, B., Getting, I. C., & Weidner, D. J. (2003). The deformation-DIA: A new apparatus for high temperature triaxial deformation to pressures up to 15 GPa. *Review of Scientific Instruments*, 74(6), 3002–3011. <https://doi.org/10.1063/1.1570948>
- Watanabe, T., Kimura, S.-I., & Karashima, S. (1984). The effect of a grain boundary structural transformation on sliding in (1010)-tilt zinc bicrystals. *Philosophical Magazine A*, 49(6), 845–864. <https://doi.org/10.1080/01418618408236566>
- Weidner, D. J., Vaughan, M. T., Wang, L., Long, H., Li, L., Dixon, N. A., & Durham, W. B. (2010). Precise stress measurements with white synchrotron X-rays. *Review of Scientific Instruments*, 81(1), 013903. <https://doi.org/10.1063/1.3263760>
- Wheeler, J., Mariani, E., Piazzolo, S., Prior, D., Trimby, P., & Drury, M. (2009). The weighted Burgers vector: A new quantity for constraining dislocation densities and types using electron backscatter diffraction on 2D sections through crystalline materials. *Journal of Microscopy*, 233(3), 482–494. <https://doi.org/10.1111/j.1365-2818.2009.03136.x>
- Wheeler, J., Prior, D., Jiang, Z., Spiess, R., & Trimby, P. (2001). The petrological significance of misorientations between grains. *Contributions to Mineralogy and Petrology*, 141(1), 109–124. <https://doi.org/10.1007/s004100000225>
- Woodhouse, J. H., Giardini, D., & Li, X.-D. (1986). Evidence for inner core anisotropy from free oscillations. *Geophysical Research Letters*, 13, 1549–1552. <https://doi.org/10.1029/g1013i013p01549>
- Wu, M. Y., & Sherby, O. D. (1984). Unification of Harper-Dorn and power law creep through consideration of internal stress. *Acta Metallurgica*, 32(9), 1561–1572. [https://doi.org/10.1016/0001-6160\(84\)90102-0](https://doi.org/10.1016/0001-6160(84)90102-0)
- Wu, M. Y., Wadsworth, J., & Sherby, O. D. (1987). Internal stress superplasticity in anisotropic. *Metallurgical Transactions A*, 18(3), 451–462. <https://doi.org/10.1007/BF02648806>
- Wuttig, M., Aning, A., & Suzuki, T. (1981). Autooscillations in zinc. *Scripta Metallurgica*, 15(11), 1237–1239. [https://doi.org/10.1016/0036-9748\(81\)90306-9](https://doi.org/10.1016/0036-9748(81)90306-9)
- Yu, W.-C., & Wen, L. (2006). Inner core attenuation anisotropy. *Earth and Planetary Science Letters*, 245(3–4), 581–594. <https://doi.org/10.1016/j.epsl.2006.03.043>
- Zou, G., Xu, Y., Li, J., Shen, Z., & Ye, L. (2024). Effect of superplastic deformation on microstructures, texture, and mechanical properties of 2A97 Al-Cu-Li alloy. *Materials Science and Engineering: A*, 891, 145972. <https://doi.org/10.1016/j.msea.2023.145972>

References From the Supporting Information

- Bramble, M. S., Flemming, R. L., & McCausland, P. J. (2015). Grain size measurement from two-dimensional micro-X-ray diffraction: Laboratory application of a radial integration technique. *American Mineralogist*, 100(8–9), 1899–1911. <https://doi.org/10.2138/am-2015-5181>
- Dobson, D. P., Hunt, S. A., & Mueller, H. J. (2012a). Slotted carbide anvils: Improved X-ray access for synchrotron-based multi-anvil experiments. *High Pressure Research*, 32(4), 532–536. <https://doi.org/10.1080/08957959.2012.746681>
- Drakopoulos, M., Connolly, T., Reinhard, C., Atwood, R., Magdysyuk, O., Vo, N., et al. (2015). I12: The joint engineering, environment and processing (JEEP) beamline at diamond light source. *Journal of Synchrotron Radiation*, 22(3), 828–838. <https://doi.org/10.1107/S1600577515003513>
- He, B. B. (2018). *Two-dimensional X-ray diffraction* (2nd ed.). John Wiley & Sons, Inc. <https://doi.org/10.1002/9781119356080>
- Hunt, S. A., & Dobson, D. P. (2017). Note: Modified anvil design for improved reliability in DT-Cup experiments. *Review of Scientific Instruments*, 88(12), 126106. <https://doi.org/10.1063/1.5005885>
- Moser, Z. (1991). The Pt-Zn (platinum-zinc) system. *Journal of Phase Equilibria*, 12(4), 439–443. <https://doi.org/10.1007/BF02645964>
- Rodríguez-Navarro, A. B., Alvarez-Lloret, P., Ortega-Huertas, M., & Rodríguez-Gallego, M. (2006). Automatic crystal size determination in the micrometer range from spotty X-ray diffraction rings of powder samples. *Journal of the American Ceramic Society*, 89(7), 2232–2238. <https://doi.org/10.1111/j.1551-2916.2006.00998.x>
- Walker, D., Carpenter, M. A., & Hitch, C. M. (1990). Some simplifications to multianvil devices for high pressure experiments. *American Mineralogist*, 75, 1020–1028.